Beyond the Classical Performance Limitations Controlling Uncertain MIMO Systems: UAV applications

Mario Garcia-Sanz, Irene Eguinoa, Jorge Elso
Automatic Control and Computer Science Department
Public University of Navarra. Campus Arrosadia
31006 Pamplona
SPAIN

E-mail: mgsanz@unavarra.es

ABSTRACT

This paper summarizes a new methodology to design sequential non-diagonal QFT controllers for multi-input-multi-output MIMO systems with uncertainty, which is a central issue in UAV control systems. It also demonstrates the feasibility of that methodology to control the position and attitude of a 6x6 MIMO spacecraft with large flexible appendages. The last part of the paper introduces a new practical methodology to design robust controllers that work under a switching mechanism, going beyond the classical linear limitations and giving a solution for the well-known robustness-performance trade-off.

1.0 INTRODUCTION

Control of multivariable systems (multiple-input-multiple-output, MIMO) with model uncertainty is still one of the hardest problems that control engineers have to face in Unmanned Air Vehicle (UAV) real-world applications. Input-output directionality, coupling among control loops, transmission zeros, pairing, etc. are some of the main complexities that define a MIMO system. Moreover, model uncertainties substantially increase such difficulties, making more restrictive the inherent performance limitations of the control system. In the last few decades a very significant amount of work in linear MIMO systems has been done. The first technique that made a quantitative synthesis of MIMO systems, taking into account quantitative bounds on the plant uncertainty and quantitative tolerances on the acceptable closed-loop system response, was the Quantitative Feedback Theory (QFT) [1]. In the last few years some new methods for non-diagonal (full matrix) multivariable QFT robust control system design have been introduced. The first part of the paper introduces a new methodology [2-6] that improves the current non-diagonal MIMO QFT control techniques. The second part validates the new techniques by applying them to control the position and attitude of a 6x6 spacecraft with large flimsy appendages [7].

Combining robust designs and stable switching, the control strategy could optimize the time response of the system by fast adaptation of the controller parameters during the transient response according to certain rules based on the amplitude of the error. The last part of the paper introduces a methodology to design a family of robust controllers able to go beyond the classical linear performance limitations. The methodology is based on both a new graphical stability criterion for switching linear systems and the robust quantitative feedback theory (QFT) [8].

2.0 NON-DIAGONAL MIMO QFT CONTROL DESIGN METHODOLOGY [2-7]

Control of multivariable systems (multiple-input-multiple-output, MIMO) with model uncertainty are still one of the hardest problems that the control engineer has to face in real-world applications. Three of the

Report Documentation Page

Form Approved
OMB No. 0704-0188

1. REPORT DATE	2. REPORT TYPE	3. DATES COVERED
MAY 2008		**00-00-2008 to 00-00-2008**

4. TITLE AND SUBTITLE	5a. CONTRACT NUMBER
Beyond the Classical Performance Limitations Controlling Uncertain MIMO Systems: UAV applications	5b. GRANT NUMBER
	5c. PROGRAM ELEMENT NUMBER
6. AUTHOR(S)	5d. PROJECT NUMBER
	5e. TASK NUMBER
	5f. WORK UNIT NUMBER
7. PERFORMING ORGANIZATION NAME(S) AND ADDRESS(ES) **Public University of Navarra Campus Arrosadia,Automatic Control and Computer Science Department,31006 Pamplona SPAIN,**	8. PERFORMING ORGANIZATION REPORT NUMBER
9. SPONSORING/MONITORING AGENCY NAME(S) AND ADDRESS(ES)	10. SPONSOR/MONITOR'S ACRONYM(S)
	11. SPONSOR/MONITOR'S REPORT NUMBER(S)

12. DISTRIBUTION/AVAILABILITY STATEMENT
Approved for public release; distribution unlimited

13. SUPPLEMENTARY NOTES
See also ADM002223. Presented at the NATO/RTO Systems Concepts and Integration Panel Lecture Series SCI-195 on Advanced Autonomous Formation Control and Trajectory Management Techniques for Multiple Micro UAV Applications held in Glasgow, United Kingdom on 19-21 May 2008.

14. ABSTRACT
See Report

15. SUBJECT TERMS

16. SECURITY CLASSIFICATION OF:			17. LIMITATION OF ABSTRACT	18. NUMBER OF PAGES	19a. NAME OF RESPONSIBLE PERSON
a. REPORT	b. ABSTRACT	c. THIS PAGE			
unclassified	**unclassified**	**unclassified**	**Same as Report (SAR)**	**43**	

main characteristics that define a MIMO system are the input and output directionality -different vectors to actuate $\boldsymbol{U}$ and to measure $\boldsymbol{Y}$-; the coupling among control loops -some outputs y_i can be influenced by several inputs u_i, and some inputs u_i can influence several outputs y_i; and the transmission zeros of the plant matrix.

In the last few decades a very significant amount of work in MIMO systems, too numerous to list here, has been done. Using MIMO QFT, Horowitz proposed to translate the original *nxn* MIMO problem into *n* separate quantitative multiple-input-single-output MISO problems, each with plant uncertainty, external disturbances and closed-loop tolerances derived from the original problem [1]. Two different approaches, the so-called sequential and non-sequential methods, consider in successive iterative steps an equivalent plant that either takes also into account the controllers designed in the previous steps, or only deals with the plant respectively.

However, although such original MIMO QFT methods take the coupling among loops into account, they only propose the use of a diagonal controller $\boldsymbol{G}$ to govern the MIMO plant. This structure can be improved using non-diagonal controllers. In fact, a fully populated matrix controller allows the designer much more design flexibility to control MIMO plants than the classical diagonal controller structure. The use of the non-diagonal components can also ease the diagonal controller design problem. In the last few years some new methods for non-diagonal multivariable QFT robust control system design have been introduced. For the sake of clarity, this section summarizes a previous work [2-7] that extends the classical QFT diagonal controller design for MIMO plants with uncertainty to the fully populated matrix controller design. The work studies three cases: the reference tracking, the external disturbance rejection at plant input and the external disturbance rejection at plant output. It presents the definition of three specific coupling matrices (c_{1ij}, c_{2ij}, c_{3ij}), one for each case, and introduces a sequential design methodology for non-diagonal QFT controllers.

2.1 The Coupling Matrix

The objective of this section is to define a measurement index (the coupling matrix) that allows one to quantify the loop interaction in MIMO control systems. Consider a *nxn* linear multivariable system -see Fig. 1-, composed of a plant $\boldsymbol{P}$, a fully populated matrix controller $\boldsymbol{G}$, a pre-filter $\boldsymbol{F}$, a plant input disturbance transfer function $\boldsymbol{P}_{di}$, and a plant output disturbance transfer function $\boldsymbol{P}_{do}$, where $\boldsymbol{P} \in \Im\mathbf{P}$, $\Im\mathbf{P}$ is the set of possible plants due to uncertainty, and,

$$\boldsymbol{P}(s)=\begin{bmatrix} p_{11}(s) & p_{12}(s) & \dots & p_{1n}(s) \\ p_{21}(s) & p_{22}(s) & \dots & p_{2n}(s) \\ \dots & \dots & \dots & \dots \\ p_{n1}(s) & p_{n2}(s) & \dots & p_{nn}(s) \end{bmatrix};\quad \boldsymbol{G}(s)=\begin{bmatrix} g_{11}(s) & g_{12}(s) & \dots & g_{1n}(s) \\ g_{21}(s) & g_{22}(s) & \dots & g_{2n}(s) \\ \dots & \dots & \dots & \dots \\ g_{n1}(s) & g_{n2}(s) & \dots & g_{nn}(s) \end{bmatrix};\quad \boldsymbol{F}(s)=\begin{bmatrix} f_{11}(s) & f_{12}(s) & \dots & f_{1n}(s) \\ f_{21}(s) & f_{22}(s) & \dots & f_{2n}(s) \\ \dots & \dots & \dots & \dots \\ f_{n1}(s) & f_{n2}(s) & \dots & f_{nn}(s) \end{bmatrix} \tag{1}$$

The reference vector $\boldsymbol{r}$' and the external disturbance vectors at plant input $\boldsymbol{d}_i$' and plant output $\boldsymbol{d}_o$' are the inputs of the system. The output vector $\boldsymbol{y}$ is the variable to be controlled.

It is denoted $\boldsymbol{P}^*$ as the plant inverse so that,

$$\boldsymbol{P}(s)^{-1} = \boldsymbol{P}^*(s) = \left[p_{ij}^*(s)\right] = \boldsymbol{\Lambda}(s) + \boldsymbol{B}(s) = \begin{bmatrix} p_{11}^*(s) & 0 & 0 \\ 0 & \cdots & 0 \\ 0 & 0 & p_{nn}^*(s) \end{bmatrix} + \begin{bmatrix} 0 & \dots & p_{1n}^*(s) \\ \dots & 0 & \dots \\ p_{n1}^*(s) & \dots & 0 \end{bmatrix} \tag{2}$$

$$\boldsymbol{G}(s)=\boldsymbol{G}_{\mathrm{d}}(s)+\boldsymbol{G}_{\mathrm{b}}(s)=\begin{bmatrix} g_{11}(s) & 0 & 0 \\ 0 & \ldots & 0 \\ 0 & 0 & g_{nn}(s) \end{bmatrix}+\begin{bmatrix} 0 & \ldots & g_{1n}(s) \\ \ldots & 0 & \ldots \\ g_{n1}(s) & \ldots & 0 \end{bmatrix} \tag{3}$$

where $\boldsymbol{\Lambda}$ is the diagonal part and $\boldsymbol{B}$ is the balance of $\boldsymbol{P}^{*}$; and $\boldsymbol{G}_{\mathrm{d}}$ is the diagonal part and $\boldsymbol{G}_{\mathrm{b}}$ is the balance of $\boldsymbol{G}$. The next paragraphs introduce a measurement index to quantify the loop interaction in the three classical cases: reference tracking, external disturbances at plant input, and external disturbances at plant output. That index is called the *coupling matrix* and, depending on the case, shows three different expressions: $\boldsymbol{C}_1$, $\boldsymbol{C}_2$, $\boldsymbol{C}_3$ respectively.

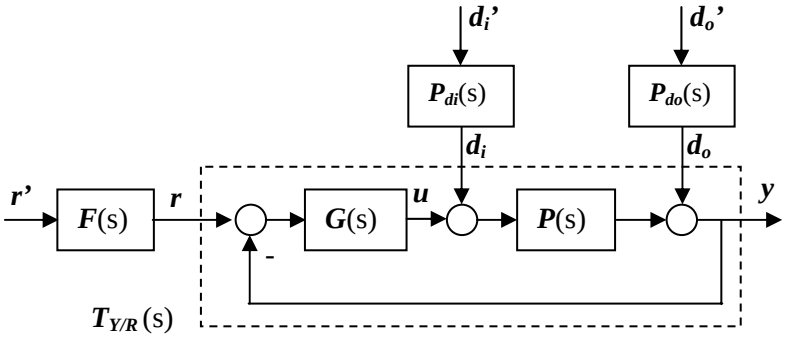

Fig. 1 Structure of a 2 Degree of Freedom MIMO System

2.1.1 Tracking

The transfer function matrix of the controlled system for the reference tracking problem, without any external disturbance, can be written as shown in Eq. (4),

$$\boldsymbol{y}=(\boldsymbol{I}+\boldsymbol{P}\,\boldsymbol{G})^{-1}\,\boldsymbol{P}\,\boldsymbol{G}\,\boldsymbol{r}=\boldsymbol{T}_{\boldsymbol{y}/\boldsymbol{r}}\;\boldsymbol{r}=\boldsymbol{T}_{\boldsymbol{y}/\boldsymbol{r}}\;\boldsymbol{F}\;\boldsymbol{r}' \tag{4}$$

Using Eq. (2) and (3), Eq. (4) can be rewritten as,

$$\boldsymbol{T}_{\boldsymbol{y}/\boldsymbol{r}}\;\boldsymbol{r}=\left(\boldsymbol{I}+\boldsymbol{\Lambda}^{-1}\,\boldsymbol{G}_{\mathrm{d}}\right)^{-1}\,\boldsymbol{\Lambda}^{-1}\,\boldsymbol{G}_{\mathrm{d}}\;\boldsymbol{r}+\left(\boldsymbol{I}+\boldsymbol{\Lambda}^{-1}\,\boldsymbol{G}_{\mathrm{d}}\right)^{-1}\,\boldsymbol{\Lambda}^{-1}\left(\boldsymbol{G}_{\mathrm{b}}\;\boldsymbol{r}-(\boldsymbol{B}+\boldsymbol{G}_{\mathrm{b}})\,\boldsymbol{T}_{\boldsymbol{y}/\boldsymbol{r}}\;\boldsymbol{r}\right) \tag{5}$$

In the expression of the closed-loop transfer function matrix of Eq. (5), it is possible to find two different terms:

i. A diagonal term $\boldsymbol{T}_{\mathrm{y/r\_d}}$,

$$\boldsymbol{T}_{\mathrm{y/r\_d}}=\left(\boldsymbol{I}+\boldsymbol{\Lambda}^{-1}\,\boldsymbol{G}_{\mathrm{d}}\right)^{-1}\,\boldsymbol{\Lambda}^{-1}\,\boldsymbol{G}_{\mathrm{d}} \tag{6}$$

that presents a diagonal structure. Note that it does not depend on the non-diagonal part of the plant inverse $\boldsymbol{B}$, nor on the non-diagonal part of the controller $\boldsymbol{G}_{\mathrm{b}}$. It is equivalent to n reference tracking SISO systems formed by plants equal to the elements of $\boldsymbol{\Lambda}^{-1}$ when the n corresponding parts of a diagonal $\boldsymbol{G}_{\mathrm{d}}$ control them, as shown in Fig. 2a.

ii. A non-diagonal term $\boldsymbol{T}_{y/r\_b}$,

$$\boldsymbol{T}_{y/r\_b} = \left(\boldsymbol{I} + \boldsymbol{\Lambda}^{-1}\,\boldsymbol{G}_d\right)^{-1}\,\boldsymbol{\Lambda}^{-1}\left[\boldsymbol{G}_b - (\boldsymbol{B}+\boldsymbol{G}_b)\,\boldsymbol{T}_{y/r}\right] = \left(\boldsymbol{I} + \boldsymbol{\Lambda}^{-1}\,\boldsymbol{G}_d\right)^{-1}\,\boldsymbol{\Lambda}^{-1}\,\boldsymbol{C}_1 \tag{7}$$

that presents a non-diagonal structure. It is equivalent to the same *n* previous systems with internal disturbances $c_{1ij}\ r_j$ at plant input (Fig. 2b).

In Eq. (7), the matrix $\boldsymbol{C}_1$ is the only part that depends on the non-diagonal parts of both the plant inverse $\boldsymbol{B}$ and the controller $\boldsymbol{G}_b$. Hence, it comprises the coupling, and from now on $\boldsymbol{C}_1$ will be the *coupling matrix* of the equivalent system for reference tracking problems,

$$\boldsymbol{C}_1 = \boldsymbol{G_b} - (\boldsymbol{B}+\boldsymbol{G_b})\,\boldsymbol{T_{y/r}} \tag{8}$$

Each element c_{1ij} of this matrix obeys,

$$c_{1ij} = g_{ij}\,(1-\delta_{ij}) - \sum_{k=1}^{n}\left(p^*_{ik} + g_{ik}\right)t_{kj}\,(1-\delta_{ik}) \tag{9}$$

where δ_{ki} is the delta of Kronecker that is defined as,

$$\delta_{ki} = \begin{cases} \delta_{ki} = 1 \Leftrightarrow k = i \\ \delta_{ki} = 0 \Leftrightarrow k \neq i \end{cases} \tag{10}$$

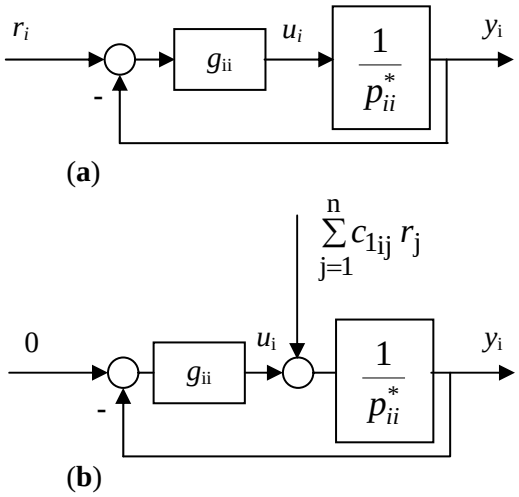

Fig. 2 i-th equivalent SISO and MISO systems

2.1.2 Disturbance rejection at plant input

The transfer matrix from the external disturbance at plant input $\boldsymbol{d}'_{\boldsymbol{i}}$ to the output $\boldsymbol{y}$ can be written as shown in Eq. (11),

$$\boldsymbol{y} = \left(\boldsymbol{I} + \boldsymbol{P}\,\boldsymbol{G}\right)^{-1} \boldsymbol{P}\,\boldsymbol{d_i} = \boldsymbol{T_{y/di}}\,\boldsymbol{d_i} = \boldsymbol{T_{y/di}}\,\boldsymbol{P_{di}}\,\boldsymbol{d_i'} \tag{11}$$

and then,

$$\boldsymbol{T}_{\mathrm{y/di}}\,\boldsymbol{d}_{\mathrm{i}} = \left(\boldsymbol{I} + \boldsymbol{\Lambda}^{-1}\,\boldsymbol{G}_{\mathrm{d}}\right)^{-1}\,\boldsymbol{\Lambda}^{-1}\,\boldsymbol{d}_{\mathrm{i}} - \left(\boldsymbol{I} + \boldsymbol{\Lambda}^{-1}\,\boldsymbol{G}_{\mathrm{d}}\right)^{-1}\,\boldsymbol{\Lambda}^{-1}\left(\left(\boldsymbol{B}+\boldsymbol{G}_{\mathrm{b}}\right)\boldsymbol{T_{y/di}}\right)\boldsymbol{d}_{\mathrm{i}} \tag{12}$$

In that expression -Eq. (12)- it is possible to find two different terms:

i. A diagonal term $\boldsymbol{T}_{\mathrm{y/di\_d}}$,

$$\boldsymbol{T}_{\mathrm{y/di\_d}} = \left(\boldsymbol{I} + \boldsymbol{\Lambda}^{-1}\,\boldsymbol{G}_{\mathrm{d}}\right)^{-1}\,\boldsymbol{\Lambda}^{-1} \tag{13}$$

Again, Eq. (13) is equivalent to *n* regulator MISO systems, as shown in Fig. 3a.

ii. Non diagonal term $\boldsymbol{T}_{\mathrm{y/di\_b}}$

$$\boldsymbol{T}_{\mathrm{y/di\_b}} = \left(\boldsymbol{I} + \boldsymbol{\Lambda}^{-1}\,\boldsymbol{G}_{\mathrm{d}}\right)^{-1}\,\boldsymbol{\Lambda}^{-1}\left(\boldsymbol{B}+\boldsymbol{G}_{\mathrm{b}}\right)\boldsymbol{T_{y/di}} = \left(\boldsymbol{I} + \boldsymbol{\Lambda}^{-1}\,\boldsymbol{G}_{\mathrm{d}}\right)^{-1}\,\boldsymbol{\Lambda}^{-1}\,\boldsymbol{C}_2 \tag{14}$$

that presents a non-diagonal structure which is equivalent to the same *n* previous systems with external disturbances $c_{2\mathrm{ij}}\,di_{\mathrm{j}}$ at plant input, as shown in Fig. 3b.

In Eq. (14), the matrix $\boldsymbol{C}_2$ comprises the coupling, and from now on $\boldsymbol{C}_2$ will be the *coupling matrix* of the equivalent system for external disturbance rejection at plant input problems,

$$\boldsymbol{C}_2 = \left(\boldsymbol{B}+\boldsymbol{G_b}\right)\boldsymbol{T_{y/di}} \tag{15}$$

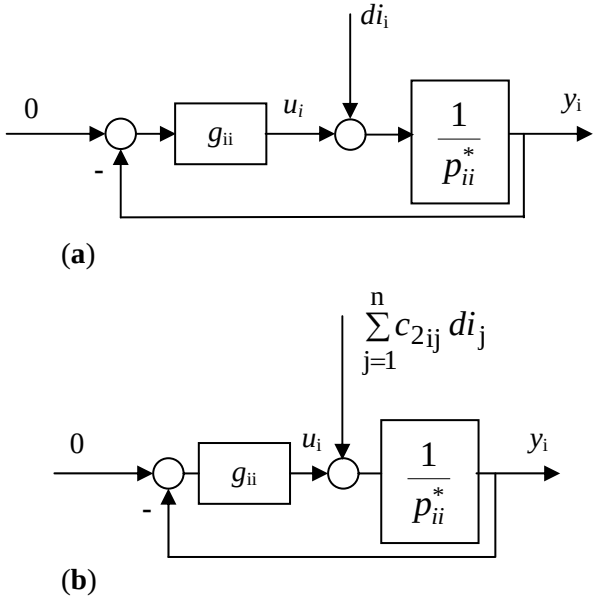

Fig. 3 i-th equivalent MISO systems

Each element c_{2ij} of this matrix obeys,

$$c_{2ij} = \sum_{k=1}^{n} (p_{ik}^{*} + g_{ik})\, t_{kj}\, (1 - \delta_{ik}) \tag{16}$$

where δ_{ki} is the delta of Kronecker defined in Equation (10).

2.1.3 Disturbance rejection at plant output

The transfer matrix from the external disturbance at plant output $\boldsymbol{d_o'}$ to the output $\boldsymbol{y}$ can be written as shown in Eq. (17),

$$\boldsymbol{y} = (\boldsymbol{I} + \boldsymbol{P}\,\boldsymbol{G})^{-1}\, \boldsymbol{d_o} = \boldsymbol{T_{y/do}}\, \boldsymbol{d_o} = \boldsymbol{T_{y/do}}\, \boldsymbol{P_{do}}\, \boldsymbol{d_o'} \tag{17}$$

and then,

$$\boldsymbol{T_{y/do}}\, \boldsymbol{d_o} = \left(\boldsymbol{I} + \boldsymbol{\Lambda}^{-1}\, \boldsymbol{G}_{\mathrm{d}}\right)^{-1}\, \boldsymbol{d_o} + \left(\boldsymbol{I} + \boldsymbol{\Lambda}^{-1}\, \boldsymbol{G}_{\mathrm{d}}\right)^{-1}\, \boldsymbol{\Lambda}^{-1}\, \left(\boldsymbol{B} - (\boldsymbol{B} + \boldsymbol{G}_{\mathrm{b}})\, \boldsymbol{T_{y/do}}\right) \boldsymbol{d_o} \tag{18}$$

In that expression -Eq. (18)- it is possible to find two different terms:

i. A diagonal term $\boldsymbol{T}_{\mathrm{y/do\_d}}$,

$$\boldsymbol{T}_{\mathrm{y/do\_d}} = \left(\boldsymbol{I} + \boldsymbol{\Lambda}^{-1}\, \boldsymbol{G}_{\mathrm{d}}\right)^{-1} \tag{19}$$

Once more, Eq. (19) is equivalent to the *n* regulator MISO systems showed in Fig. 4a,

ii. Non diagonal term $\boldsymbol{T}_{\mathrm{y/do\_b}}$

$$\boldsymbol{T}_{\mathrm{y/do\_b}} = \left(\boldsymbol{I} + \boldsymbol{\Lambda}^{-1}\, \boldsymbol{G}_{\mathrm{d}}\right)^{-1}\, \boldsymbol{\Lambda}^{-1}\, \left[\boldsymbol{B} - (\boldsymbol{B} + \boldsymbol{G}_{\mathrm{b}})\, \boldsymbol{T_{y/do}}\right] = \left(\boldsymbol{I} + \boldsymbol{\Lambda}^{-1}\, \boldsymbol{G}_{\mathrm{d}}\right)^{-1}\, \boldsymbol{\Lambda}^{-1}\, \boldsymbol{C}_3 \tag{20}$$

that presents a non-diagonal structure. It is equivalent to the same *n* previous systems with external disturbances $c_{3ij}\, do_j$ at plant input, as shown Fig. 4b.

In Eq. (20), the matrix $\boldsymbol{C}_3$ comprises the coupling, and from now on it will be the *coupling matrix* of the equivalent system for external disturbance rejection at plant output problems,

$$\boldsymbol{C}_3 = \boldsymbol{B} - (\boldsymbol{B} + \boldsymbol{G}_b)\, \boldsymbol{T_{y/do}} \tag{21}$$

Each element of the coupling matrix, c_{3ij} obeys,

$$c_{3ij} = p_{ij}^{*}\, (1 - \delta_{ij}) - \sum_{k=1}^{n} (p_{ik}^{*} + g_{ik})\, t_{kj}\, (1 - \delta_{ik}) \tag{22}$$

where δ_{ki} is the delta of Kronecker as defined in Equation (10).

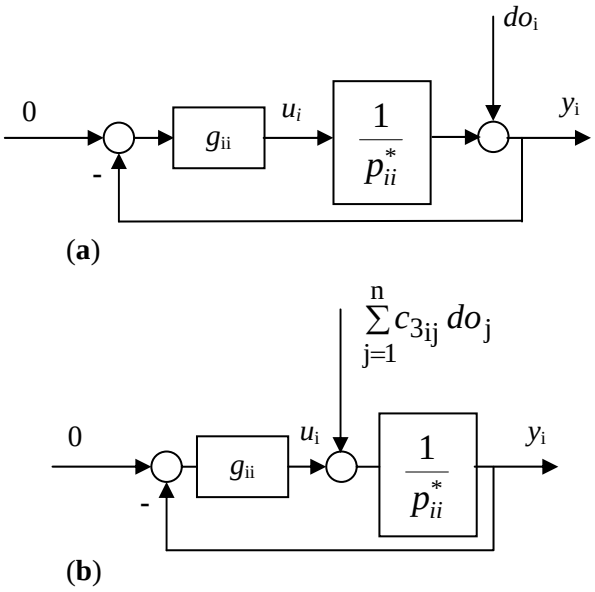

Fig. 4 i-th equivalent MISO systems

2.2 The Coupling Elements

In order to design a MIMO controller with a low coupling level, it is necessary to study the influence of every non-diagonal element g_{ij} on the coupling elements c_{1ij}, c_{2ij} and c_{3ij}, defined in Eq. (9), (16) and (22). These elements can be simplified to quantify the coupling effects. Then it will be possible to analyze the loop decoupling and to state some conditions and limitations using fully populated matrix controllers. To analyze the coupling elements, one Hypothesis is stated.

Hypothesis H1: suppose that in Eq. (9), (16) and (22),

$$\left|\left(p^*_{ij}+g_{ij}\right)t_{jj}\right| >> \left|\left(p^*_{ik}+g_{ik}\right)t_{kj}\right|,\ \text{for } k \neq j, \text{ and in the bandwidth of } t_{jj} \qquad \textbf{(23)}$$

Note that the above expression is scale invariant and is typically fulfilled once the MIMO system has been ordered according to appropriate methods like the Relative Gain Analysis, etc. Then the diagonal elements t_{jj} will be much larger that the non-diagonal ones t_{kj},

$$\left|t_{jj}\right| >> \left|t_{kj}\right|,\ \text{for } k \neq j, \text{ and in the bandwidth of } t_{jj} \qquad \textbf{(24)}$$

Now, two simplifications are applied to facilitate the quantification of the coupling effects c_{1ij}, c_{2ij}, c_{3ij}.

Simplification S1: Using the Hypothesis H1, Eqs. (9), (16) and (22), which describe the coupling elements in the tracking problem, disturbance rejection at plant input and disturbance rejection at plant output respectively, are rewritten as shown Table I.

Simplification S2: The elements t_{jj} are computed for each case from the equivalent system derived from Eqs. (6), (13) and (19). The results are shown in Table I.

Table I. Simplifications to quantify the coupling effects

	Reference tracking	*External disturbances at plant input*	*External disturbances at plant output*
Simplification S1	$c_{1ij} = g_{ij} - t_{jj}\left(p^*_{ij} + g_{ij}\right)\ ;\ i \neq j$ **(25)**	$c_{2ij} = t_{jj}\left(p^*_{ij} + g_{ij}\right)\ ;\ i \neq j$ **(26)**	$c_{3ij} = p^*_{ij} - t_{jj}\left(p^*_{ij} + g_{ij}\right)\ ;\ i \neq j$ **(27)**
Simplification S2	$t_{jj} = \dfrac{g_{jj}\ p^{*-1}_{jj}}{1 + g_{jj}\ p^{*-1}_{jj}}$ **(28)**	$t_{jj} = \dfrac{p^{*-1}_{jj}}{1 + g_{jj}\ p^{*-1}_{jj}}$ **(29)**	$t_{jj} = \dfrac{1}{1 + g_{jj}\ p^{*-1}_{jj}}$ **(30)**

Due to Simplifications S1 and S2, the coupling effects c_{1ij}, c_{2ij}, c_{3ij} can be computed as,

Tracking

$$c_{1ij} = g_{ij} - \frac{g_{jj}\left(p^*_{ij} + g_{ij}\right)}{\left(p^*_{jj} + g_{jj}\right)} \quad ; \quad i \neq j \tag{31}$$

Disturbance rejection at plant input

$$c_{2ij} = \frac{\left(p^*_{ij} + g_{ij}\right)}{\left(p^*_{jj} + g_{jj}\right)} \quad ; \quad i \neq j \tag{32}$$

Disturbance rejection at plant output

$$c_{3ij} = p^*_{ij} - \frac{p^*_{jj}\left(p^*_{ij} + g_{ij}\right)}{\left(p^*_{jj} + g_{jj}\right)} \quad ; \quad i \neq j \tag{33}$$

2.3 The Optimum Non-diagonal Controller

Consider non-diagonal controllers to reduce the coupling effect and diagonal controllers that help to achieve the loop performance specifications. The optimum non-diagonal controllers for the three cases (tracking and disturbance rejection at plant input and output) can be obtained making the loop interaction of Eqs. (31), (32) and (33) equal to zero.

Note that both elements, p^*_{ij} and p^*_{jj}, of these equations are uncertain elements of $\boldsymbol{P}^*$. Every uncertain plant p^*_{ij} can be any plant represented by the family,

$$\left\{p^*_{ij}\right\} = p^{*N}_{ij}\left(1 + \Delta_{ij}\right)\ ,\ 0 \leq \left|\Delta_{ij}\right| \leq \Delta\, p^*_{ij}\ ,\ \text{for i, j} = 1,...,n \tag{34}$$

where p^{*N}_{ij} is the nominal plant, and Δp^*_{ij} the maximum of the non-parametric uncertainty radii $\left|\Delta_{ij}\right|$.

The nominal plants p^{*N}_{ij} and p^{*N}_{jj} that will be chosen for the optimum non-diagonal controller will

follow the next rules:

a) If the uncertain parameters of the plants show a uniform Probability Distribution (Fig. 5a) –which is typical in the QFT methodology-, then the elements p_{ij}^{*} and p_{jj}^{*} for the optimum non-diagonal controller will be the nominal plants p_{ij}^{*N} and p_{jj}^{*N}, which minimise the maximum of the non-parametric uncertainty radii Δp_{ij}^{*} and Δp_{jj}^{*} that comprise the plant templates (Fig. 5b).

b) If the uncertain parameters of the plants show a non-uniform Probability Distribution (Fig. 5c), then the elements p_{ij}^{*} and p_{jj}^{*} for the optimum non-diagonal controller will be the nominal plants p_{ij}^{*N} and p_{jj}^{*N}, whose set of parameters maximize the area of the Probability Distribution in the regions $[\,a_{ij}-\varepsilon\,,a_{ij}+\varepsilon\,]$ and $[\,a_{jj}-\varepsilon\,,a_{jj}+\varepsilon\,]$ ($\forall$ parameter a_{ij}, b_{ij}, …, a_{jj}, b_{jj} …) respectively.

Now, making Eqs. (31), (32) and (33) equal to zero and using Eq. (34), the optimum non-diagonal controller for each case is obtained.

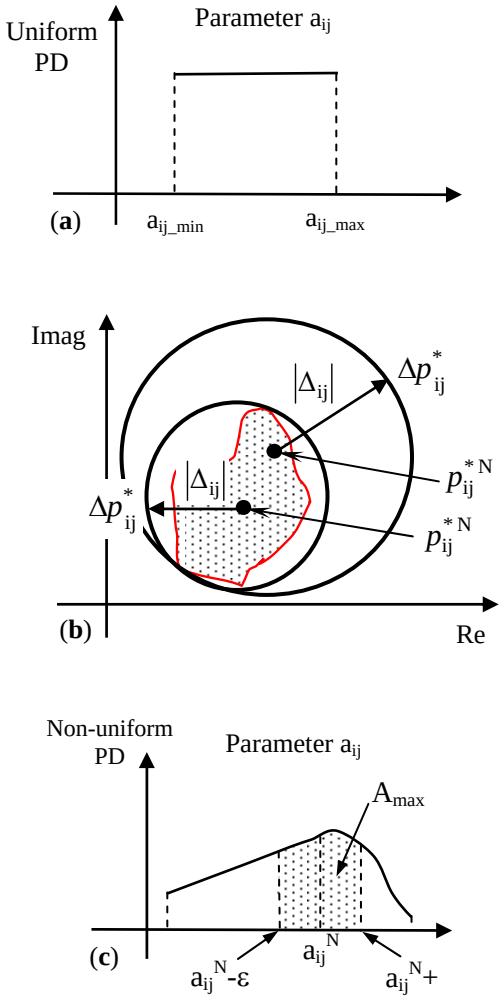

Fig. 5 Probability Distribution of the parameter a_{ij}, and Non-parametric uncertainty radii Δp_{ij}^{*} that comprise the plant templates

2.3.1 Tracking

$$g_{ij}^{opt} = F_{pd}\left(g_{jj} \frac{p_{ij}^{*N}}{p_{jj}^{*N}} \right), \text{for } i \neq j \quad \textbf{(35)}$$

2.3.2 Disturbance rejection at plant input

$$g_{ij}^{opt} = F_{pd}\left(- p_{ij}^{*N} \right), \text{for } i \neq j \quad \textbf{(36)}$$

2.3.3 Disturbance rejection at plant output

$$g_{ij}^{opt} = F_{pd}\left(g_{jj} \frac{p_{ij}^{*N}}{p_{jj}^{*N}} \right), \text{for } i \neq j \quad \textbf{(37)}$$

where the function $F_{pd}(A)$ means in every case a casual and stable proper function made from the dominant poles and zeros of the expression A.

2.4 The Coupling Effects

The minimum achievable coupling effects -Eqs. (38), (40), (42)- can be computed substituting the optimum controller of Eqs. (35), (36) and (37) in the coupling expressions of Eqs. (31), (32) and (33) respectively, and taking into account the uncertainty radii of Eq. (34). Analogously, the maximum coupling effect without any non-diagonal controller -pure diagonal controller cases- can be computed substituting g_{ij}=0 in the Eqs. (31), (32) and (33) respectively -Eqs. (39), (41), (43)-. That is to say,

2.4.1 Tracking

$$\left| c_{1ij} \right|_{g_{ij}=g_{ij}^{opt}} = \left| \psi_{ij} \left(\Delta_{jj} - \Delta_{ij} \right) g_{jj} \right| \quad \textbf{(38)}$$

$$\left| c_{1ij} \right|_{g_{ij}=0} = \left| \psi_{ij} \left(1 + \Delta_{ij} \right) g_{jj} \right| \quad \textbf{(39)}$$

2.4.2 Disturbance rejection at plant input

$$\left| c_{2ij} \right|_{g_{ij}=g_{ij}^{opt}} = \left| \psi_{ij} \ \Delta_{ij} \right| \quad \textbf{(40)}$$

$$\left| c_{2ij} \right|_{g_{ij}=0} = \left| \psi_{ij} \left(1 + \Delta_{ij} \right) \right| \quad \textbf{(41)}$$

2.4.3 Disturbance rejection at plant output

$$\left| c_{3ij} \right|_{g_{ij}=g_{ij}^{opt}} = \left| \psi_{ij} \left(\Delta_{ij} - \Delta_{jj} \right) g_{jj} \right| \quad \textbf{(42)}$$

$$\left| c_{3ij} \right|_{g_{ij}=0} = \left| \psi_{ij} \left(1 + \Delta_{ij} \right) g_{jj} \right| \quad \textbf{(43)}$$

where,

$$\psi_{ij} = \frac{p_{ij}^{*N}}{\left(1+\Delta_{jj}\right) p_{jj}^{*N} + g_{jj}} \qquad \textbf{(44)}$$

and the uncertainty is: $0 \le \left|\Delta_{ij}\right| \le \Delta\, p_{ij}^{*}$, $0 \le \left|\Delta_{jj}\right| \le \Delta\, p_{jj}^{*}$, for i, j = 1,..., n

The coupling effects, calculated in the pure diagonal controller cases, result in three expressions (39), (41) and (43) that still present a non-zero value when the nominal-actual plant mismatching due to the uncertainty disappears: $\Delta_{ij} = 0$ and $\Delta_{jj} = 0$. However, the coupling effects obtained with the optimum non-diagonal controllers -Eqs. (38), (40) and (42)- tends to zero when that mismatching disappears.

2.5 Design Methodology

The proposed controller design methodology is a sequential procedure closing loops with four steps [2-7]:

Step A: Controller structure, input-output pairing and loop ordering. First, the methodology identifies the controller structure (minimum required elements of the controller matrix) and the input-output pairings by using the frequency-dependent Relative Gain Array –RGA- [10-11]. Then, the matrix $\boldsymbol{P}^{*}(s)$ is reorganized so that $[p_{11}^{*}(s)]^{-1}$ has the smallest phase margin frequency, $[p_{22}^{*}(s)]^{-1}$ the next smallest phase margin frequency, and so on to guarantee the existence of a solution [1].

After that, the sequential design technique composed of *n* stages, as many as loops, performs the following two steps *B* and *C* for every column of the matrix compensator $\boldsymbol{G}(s)$ from $k = 1$ to n (Fig. 6).

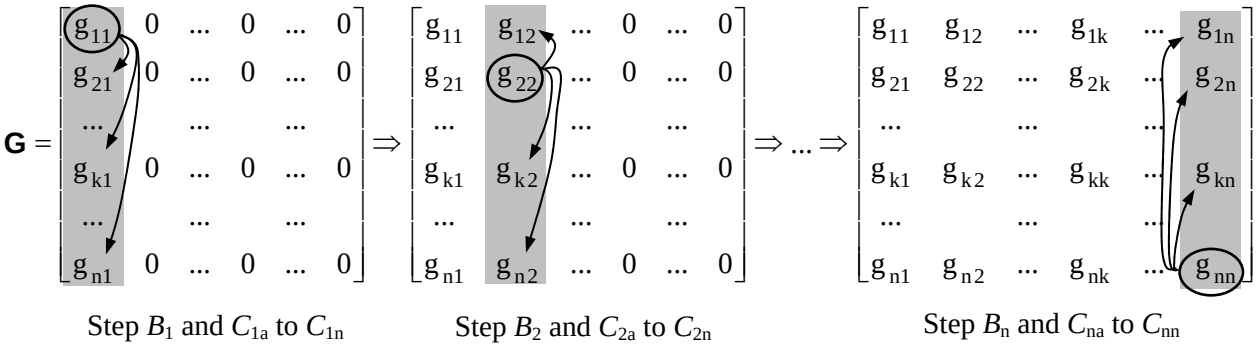

Fig. 6 Steps for controllers design

Step B: Design of the diagonal compensator $g_{kk}(s)$. The diagonal element $g_{kk}(s)$ is calculated through standard QFT loop-shaping [1] for the inverse of the equivalent plant $[p_{kk}^{*e}(s)]_k^{-1}$ in order to achieve robust stability and robust performance specifications [13-14]. The equivalent plant satisfies the recursive relationship (45) [13], which is an extension for the non-diagonal case of the recursive expression proposed by Horowitz [12] as the *Improved design technique*, also called *Second method* by Houpis *et al.* [1].

$$\left[p_{ij}^{*e}(s)\right]_k = \left[p_{ij}^{*e}(s)\right]_{k-1} - \frac{\left(\left[p_{i(k-1)}^{*e}(s)\right]_{k-1} + \left[g_{i(k-1)}(s)\right]_{k-1}\right)\left(\left[p_{(k-1)j}^{*e}(s)\right]_{k-1} + \left[g_{(k-1)j}(s)\right]_{k-1}\right)}{\left[p_{(k-1)(k-1)}^{*e}(s)\right]_{k-1} + \left[g_{(k-1)(k-1)}(s)\right]_{k-1}};$$

$$\text{i, j} \ge \text{k}; \quad \left[\boldsymbol{P}^{*e}(s)\right]_{k=1} = \boldsymbol{P}^{*}(s) \qquad \textbf{(45)}$$

If the control system requires tracking specifications as $a_{ii}(\omega) \le \left| t_{ii}^{y/r}(j\omega) \right| \le b_{ii}(\omega)$ then, because $t_{ii}^{y/r} = t_{rii} + t_{c1ii}$ -Eq.(5)-, the tracking bounds b_{ii} and a_{ii} will have to be corrected with the coupling specification τ_{c1ii}, so that:

$$b_{ii}^{c} = b_{ii} - \tau_{c1ii} \quad , \quad a_{ii}^{c} = a_{ii} + \tau_{c1ii} \tag{46}$$

$$t_{c1ii} = w_{ii}\ c_{1ii} \le \tau_{c1ii} \tag{47}$$

$$a_{ii}^{c}(\omega) \le |t_{rii}(j\omega)| \le b_{ii}^{c}(\omega) \tag{48}$$

These are the same corrections proposed originally by Horowitz (see also [1]). However, with the proposed non-diagonal method these corrections will be less demanding. The coupling expression $t_{c1ii} = w_{ii}\ c_{1ii}$ is now minor than in the previous diagonal methods –compare Eqs. (38) and (39)-. The off-diagonal elements g_{ij} (i≠j) of the matrix controller will attenuate or cancel that cross coupling. Then the diagonal elements g_{kk} of the non-diagonal method will need less bandwidth than the diagonal elements of the previous diagonal methods.

Step C: Design of the (n-1) non-diagonal elements $g_{ik}(s)$ ($i \neq k$, $i = 1,2,...n$). The $g_{ik}(s)$ (i ≠ k) elements of the *k*-th compensator column are designed to minimize the non-diagonal elements of the cross-coupling matrices according to different purposes: reference tracking (31), (35); disturbance rejection at plant input (32), (36); and disturbance rejection at plant output (33), (37). The resulting compensators $g_{ik}(s)$ have to be casual and stable, and include the dominant dynamics.

The off-diagonal controller elements can be allocated not only to reduce the coupling effects of the MIMO system, but also to reach complementary objectives, such as to remove RHP (right-half plane) transmission zeros introduced during the controller design [5], improve system integrity [13] and stability margins, reduce controller efforts, etc.

Step D: Design of the prefilter. The design of the prefilter $\boldsymbol{F}(s)$ does not present any additional difficulty because the final transfer function that relates $\boldsymbol{R}(s)$ to $\boldsymbol{Y}(s)$ shows less loop interaction thanks to the fully populated compensator design. Therefore, the prefilter $\boldsymbol{F}(s)$ can generally be a diagonal matrix.

2.6 Stability Conditions

Closed-loop stability of a MIMO system with a non-diagonal controller designed by using a sequential procedure is guaranteed by the following sufficient conditions [14]:

(c.1) each $L_i(s) = g_{ii}(s)\ [p_{ii}^{*e}(s)]_i^{-1}$, i=1, ..., *n*, satisfies the Nyquist encirclement condition,

(c.2) no RHP pole-zero cancellations occur between $g_{ii}(s)$ and $[p_{ii}^{*e}(s)]_i^{-1}$, i=1,...,*n*,

(c.3) no Smith-McMillan pole-zero cancellations occur between $\boldsymbol{P}(s)$ and $\boldsymbol{G}(s)$, and

(c.4) no Smith-McMillan pole-zero cancellations occur in $\left| \boldsymbol{P}^{*}(s) + \boldsymbol{G}(s) \right|$.

2.7 Remarks

It is important to note that the calculation of the equivalent plant $[p_{kk}^{*e}(s)]_k^{-1}$, (45), usually introduces some exact pole-zero cancellations. That operation could be precisely performed by using symbolic mathematical tools [1]. However, fictitious poles and zeros may be introduced when using numerical

calculus due to the typical rounding errors of the computer. Additionally, it is needed to determine the inverse of the plant matrix, which can also be numerically non-reliable.

In this paper, these problems are overcome through a new frequency response computation method. That is, for each frequency of interest ω and for every set of parameters within the region of uncertainty, each element $p_{ij}(j\omega)$ of the plant transfer function matrix is translated into a complex matrix $\boldsymbol{P}_{freq\_ij}$ that represents the frequency response of every plant element within the uncertainty. Thus, this complex matrix has as many rows as different cases generated due to the uncertainty and as many columns as frequencies (49). All the abovementioned calculations are then performed on the basis of this set of complex matrices by using element-by-element matrix operations. As a result, potential impediments related to practical computation are avoided.

$$\boldsymbol{P}_{freq\_ij} = \begin{array}{c} \text{frequencies} \Rightarrow \\ \text{Case 1} \\ \text{Case 2} \\ \vdots \\ \text{Case } k \\ \vdots \\ \text{Case } m \end{array} \begin{array}{c} \begin{bmatrix} \omega_1 & \omega_2 & \cdots & \omega_r & \cdots & \omega_n \\ a_{11} & a_{12} & \cdots & & \cdots & a_{1n} \\ a_{21} & \cdots & \cdots & & \cdots & \cdots \\ \cdots & \cdots & \cdots & & \cdots & \cdots \\ \cdots & \cdots & \cdots & & \cdots & \cdots \\ a_{m1} & \cdots & \cdots & & \cdots & a_{mn} \end{bmatrix} \\ \text{Template at } \omega_r \end{array} \quad \text{Plant } k \tag{49}$$

$$a_{kr} = \mathrm{Re}(a_{kr}) + j\,\mathrm{Imag}(a_{kr})$$

At the same time, arbitrarily picking the wrong order of the loops to be designed can result in the non-existence of a solution. This may occur if the solution process is based on satisfying an upper limit of the phase margin frequency ω_ϕ, for each loop. Hence, Loop *i* having the smallest phase margin frequency will have to be chosen as the first loop to be designed. The loop that has the next smallest phase margin frequency will be next, and so on [1].

Although very remote, theoretically there exists the possibility of introducing RHP transmission zeros due to the compensator design. This undesirable situation can not be detected until the multivariable system design is completed. To avoid it the proposed methodology (Steps *A, B* and *C*) is inserted in a procedure introduced by Garcia-Sanz and Eguinoa [5]. Once the matrix compensator $\boldsymbol{G}(s)$ is designed, the transmission zeros of $\boldsymbol{P}(s)\,\boldsymbol{G}(s)$ are determined using the Smith-McMillan form and over the set of possible plants $\Im\mathbf{P}$ due to uncertainty. If there exist new RHP transmission zeros apart from those initially present in $\boldsymbol{P}(s)$, they can be removed by using the non-diagonal elements placed in the last column of the matrix $\boldsymbol{G}(s)$.

3.0 MIMO QFT CONTROL FOR A SPACECRAFT WITH LARGE FLEXIBLE APPENDAGES [7]

This section summarizes the design of a robust non-diagonal MIMO QFT controller to govern the position and attitude of a Darwin-type spacecraft with large flexible appendages. The satellite is one of the flyers of a multiple spacecraft constellation for a future ESA mission. It presents a 6x6 high order MIMO model with large uncertainty and loop interactions introduced by the flexible modes of the low-stiffness appendages. The scientific objectives of the satellite require very demanding control specifications for position and attitude accuracy, high disturbance rejection, loop-coupling attenuation and low order controller. This section demonstrates the feasibility of sequential non-diagonal MIMO QFT strategies

controlling the Darwin spacecraft and compares the results with a previous H-infinity design.

3.1 Description

The Darwin mission consists of three to six telescopes arranged in a symmetric configuration flying in formation around a master satellite or central hub (Fig. 7). Darwin will employ nulling interferometry to detect and analyze through appropriate spectroscopy techniques the atmosphere of remote planets close to a bright star. The infrared light collected by the free flying telescopes will be recombined inside the hub-satellite in such a way that the light from the central star suffers destructive interference and is cancelled out, allowing this way the much fainter planet easier to stand out. The interferometry requires very accurate and stable positioning of the spacecraft in the constellation, which puts high demands on the attitude and position control system. Darwin will be placed further away, at a distance of 1.5 million kilometers from Earth, in the opposite direction from the Sun (Earth-Sun Lagrangian Point L2 –Fig.8).

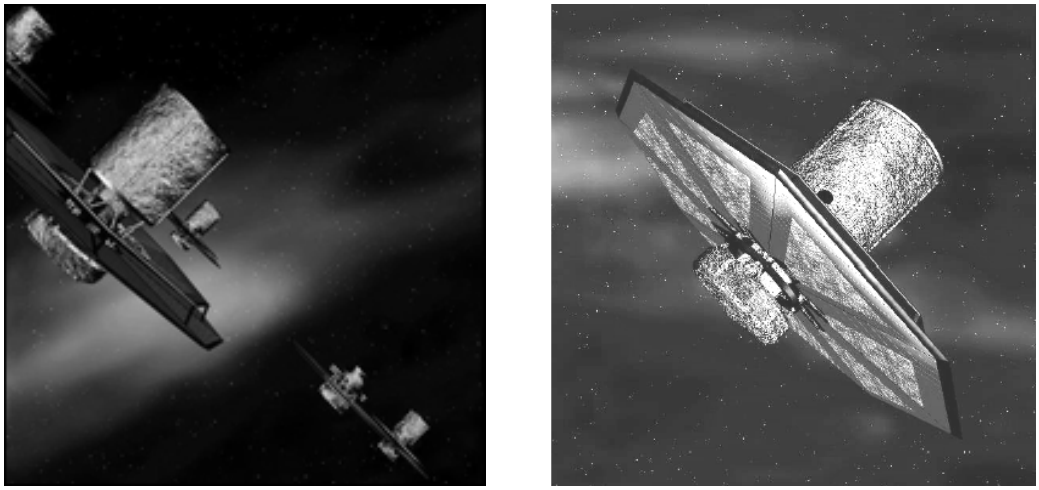

Fig. 7 Darwin spacecraft (Artist's view. ESA courtesy)

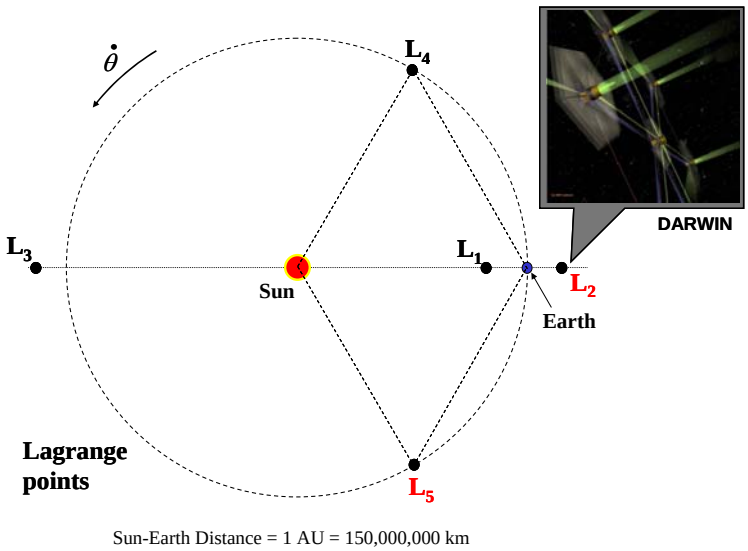

Fig. 8 Earth-Sun Lagrangian Points and Darwin spacecraft location

Each telescope flyer is cylindrically shaped (2 m diameter, 2 m height) and weighs 500 kg. In order to protect the instrument from the sunlight, it is equipped with a sunshield modeled with 6 large flexible

beams (4 m long and 7 kg) attached to the rigid structure (Fig. 9; beam end-point coordinates in brackets). The main mechanical characteristics of the Darwin-type Flyer are summarized in Table II.

For every beam (Fig. 9), two different frequencies for the first modes along Y and Z beam axes are considered. Their frequency can vary from 0.05 Hz to 0.5 Hz, with a nominal value of 0.1 Hz, and their damping can vary from 0.1% to 1%, with a nominal value of 0.5%. As regards spacecraft mass and inertia, the corresponding uncertainty around their nominal value is of 5%.

Based on the previous description and using a mechanical modeling formulation for multiple flexible appendages of a rigid body spacecraft, the open-loop transfer function matrix representation of the Darwin-type Flyer is given in (50) and Fig. 10:

$$\begin{bmatrix} x(s) \\ y(s) \\ z(s) \\ \varphi(s) \\ \theta(s) \\ \psi(s) \end{bmatrix} = \boldsymbol{P}(s)\,\boldsymbol{U}(s) = \begin{bmatrix} p_{11}(s) & p_{12}(s) & p_{13}(s) & p_{14}(s) & p_{15}(s) & p_{16}(s) \\ p_{21}(s) & p_{22}(s) & p_{23}(s) & p_{24}(s) & p_{25}(s) & p_{26}(s) \\ p_{31}(s) & p_{32}(s) & p_{33}(s) & p_{34}(s) & p_{35}(s) & p_{36}(s) \\ p_{41}(s) & p_{42}(s) & p_{43}(s) & p_{44}(s) & p_{45}(s) & p_{46}(s) \\ p_{51}(s) & p_{52}(s) & p_{53}(s) & p_{54}(s) & p_{55}(s) & p_{56}(s) \\ p_{61}(s) & p_{62}(s) & p_{63}(s) & p_{64}(s) & p_{65}(s) & p_{66}(s) \end{bmatrix} \begin{bmatrix} F_x(s) \\ F_y(s) \\ F_z(s) \\ T_\varphi(s) \\ T_\theta(s) \\ T_\psi(s) \end{bmatrix} \quad \textbf{(50)}$$

where x, y, z are the position coordinates; φ, θ, ψ are the corresponding attitude angles; F_x, F_y, F_z are the force inputs; T_φ, T_θ, T_ψ are the torque inputs; and where every $p_{ij}(s)$, i, j = 1,…,6, is a 50th order Laplace transfer function with uncertainty.

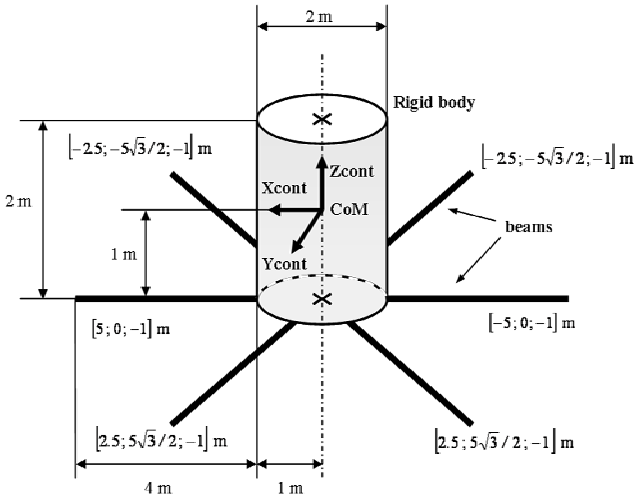

Fig. 9 Darwin type 6 DOF satellite model

The Bode diagram of the plant (Fig. 10) shows the dynamics of the 36 matrix elements. Each of them and the MIMO system (matrix) are minimum phase. The flexible modes introduced by the appendages (second-order dipoles) affect all the elements around the frequencies ω = [0.19, 10] rad/sec. The diagonal elements $p_{ii}(s)$, i = 1,…,6, and the elements $p_{15}(s)$, $p_{51}(s)$, $p_{24}(s)$ and $p_{42}(s)$ are mainly double integrators plus the flexible modes.

Table II. Mechanical characteristics of the Darwin-type Flyer model

Parameter	Value
Satellite body mass	500 kg
Cylinder dimensions	2 m diameter, 2 m height
Inertia tensor of satellite in control frame at satellite Centre of Mass (without reflector)	$\left[\boldsymbol{I}_{\text{Darwin\_body}}\right]_{\text{CoM}}\big\vert_{\text{Cont}} = \begin{bmatrix} 250 & 0 & 0 \\ 0 & 250 & 0 \\ 0 & 0 & 250 \end{bmatrix} \text{kg}\cdot\text{m}^2$
Inertia tensor of satellite in control frame at satellite Centre of Mass (with reflector)	$\left[\boldsymbol{I}_{\text{Darwin\_body}}\right]_{\text{CoM}}\big\vert_{\text{Cont}} = \begin{bmatrix} 509 & 0 & 0 \\ 0 & 509 & 0 \\ 0 & 0 & 684 \end{bmatrix} \text{kg}\cdot\text{m}^2$
Position of Centre of Mass in control frame at satellite Centre of Mass	[0, 0, 0] m
Sunshield mass	7 kg * 6 beams = 42 kg
Beam length	4 m

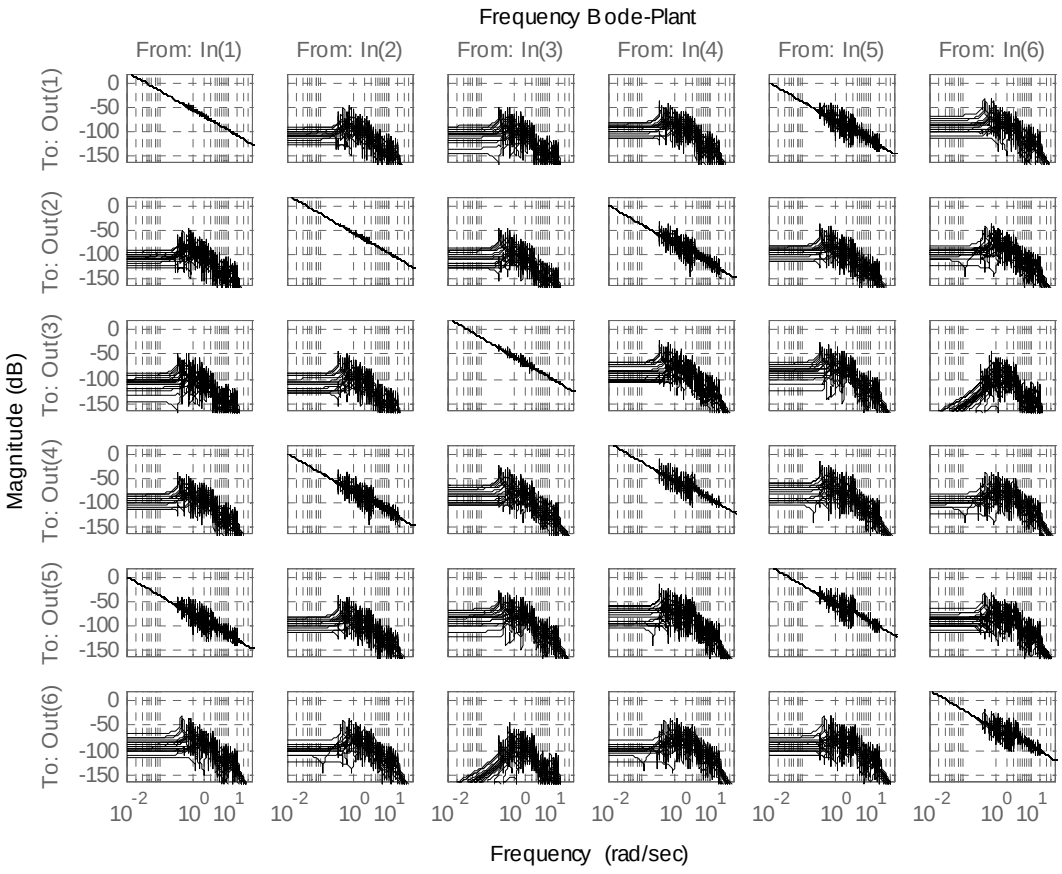

Fig. 10 Darwin-type flyer dynamics

The block diagram of the control system is shown in Fig. 11. The sensor module represents both the OPD (Optical Pathlength Differences) Fringe Tracker sensor and the FPM (Fine Pointing Metrology) sensor, which measure the satellite position and attitude, respectively. The actuators, FEEP (Field Emission Electric Propulsion) thrusters, are a type of electrostatic propulsion that provides very small and precise actuation (Table III).

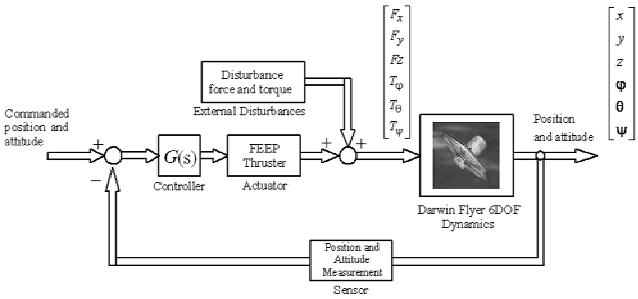

Fig. 11 General 6x6 satellite control loop

The external disturbances acting on the satellite (gravity gradient and solar pressure), although very small, are also modeled as forces and torques along the 3 axes. The gravity gradient is modeled as a constant bias and the solar pressure is represented as a white noise perturbation (Table III).

Table III. Characteristics of sensors, actuators and external disturbances

Name	Characteristics	Values
Fine Pointing Metrology (FPM)	For very precise relative attitude measurements $\theta_{meas} = \theta_{true} + WN_{FPM}$	WN_{FPM} = Attitude white noise. PSD of 10.66 mas/$\sqrt{Hz}$ along the 3 axes Attitude range:[-40; 40] arcsec Sampling frequency: 1Hz
Optical Pathlength Differences (OPD) Fringe Tracker	For precise 3-axis measure of position $X_{meas} = X_{true} + WN_{OPD}$	WN_{OPD} = Position white noise. PSD of 2 nm/$\sqrt{Hz}$ along the 3 axes Attitude range:[-1; 1] µm Sampling frequency: 1Hz
FEEPS actuators	For very small and precise actuation $F_{FEEP} = F_{commanded} + WN_{FEEP}$ $T_{FEEP} = T_{commanded} + WN_{T\_FEEP}$	*Force model:* WN_{FEEP} = Force white noise. PSD of 0.1 µN / $\sqrt{Hz}$ along the 3 axes, which can eventually vary up to 0.5 µN / $\sqrt{Hz}$. Force range:[-150; 150] µN *Torque model:* WN_{T_FEEP} = Torque white noise. PSD of 0.1 µNm / $\sqrt{Hz}$ along the 3 axes, which can eventually vary up to 0.5 µNm / $\sqrt{Hz}$. Torque range:[-150; 150] µNm Sampling frequency: 1Hz
Solar Pressure	$F_{Sun} = B_{F\_Sun} + W_{NF\_Sun}$ $T_{Sun} = B_{T\_Sun} + W_{NT\_Sun}$	*Force model:* W_{NF_Sun} = Force white noise. PSD of 0.05 µN / $\sqrt{Hz}$ along the 3 axes B_{F_Sun} = 10 µN *Torque model:* W_{NT_Sun} = Torque white noise. PSD of 0.1 µNm / $\sqrt{Hz}$ along the 3 axes B_{T_Sun} = 10 µNm
Gravity Gradient	F_{Grav} T_{Grav}	*Force model:* F_{Grav} = 0.03 µN along the 3 axes *Torque model:* T_{Grav} = 0.03 µNm along the 3 axes

θ = attitude. X = position. F = Force. T = Torque

The original dynamics benchmark simulator, provided by ESA and implemented under Matlab/Simulink, integrates all those elements constituting the whole satellite control system: sensors, actuators, dynamics, disturbances, etc. (Fig. 11). For each performance evaluation campaign, 300 random dynamics within the uncertainty (Monte-Carlo analysis) are generated to evaluate the performance of the controllers.

Table IV. Darwin-type Flyer requirements

	Objective	Numerical Requirement
Astronomical Requirements	Position accuracy	Maximum absolute value: 1 μm for all axes
		Standard deviation: 0.33 μm for all axes
	Pointing accuracy	Maximum absolute value: 25.5 mas for all axes (3 σ)
		Standard deviation: 8.5 mas for all axes (1 σ)
Engineering Requirements	Bandwidth	~ 0.01 Hz for all axes
	Saturation limits	Maximum force: 150 μN Maximum torque: 150 μNm
	Rejection of high frequency noises (from measurement and actuation)	High roll-off after the bandwidth
Control Requirements	Stability margins	$\max_{\omega}\lvert \boldsymbol{T}(j\omega)\rvert < 2$ $\max_{\omega}\lvert \boldsymbol{S}(j\omega)\rvert < 2$
	Loop interaction	Minimum
	Rejection of flexible modes	Maximum
	Controller complexity and order	Minimum

3.2 Control objectives

The main objective of the spacecraft is to fulfill some astronomical requirements that demand to keep the flying telescope pointing at both the observed space target and the central hub-satellite. This set of specifications leads to some additional engineering requirements (bandwidth, saturation limits, noise rejection, etc.) and also needs some complementary control requirements (stability, low loop interaction, low controller complexity and order, etc.) –Table IV-.

3.3 Non-diagonal MIMO QFT Controller Design

The sequential non-diagonal MIMO QFT methodology previously described in Section 2 [2-7] is applied here to control the position and attitude of the Darwin-type Flyer.

3.3.1 Relative Gain Array Interaction Analysis –Step A-

The Relative Gain Array (RGA) of a non-singular square matrix $\boldsymbol{P}$ is a scale-invariant measure of interactions. Its original definition introduced by Bristol [11] was only proposed for steady state (ω = 0 rad/sec). However, the RGA can also be computed frequency-by-frequency (51) and used to assess the interaction at frequencies other than zero [10]. In most cases, the value of RGA at frequencies close to crossover is the most important one.

$$RGA(j\omega) = \left[\lambda_{ij}(j\omega)\right] = \boldsymbol{P}(j\omega) \otimes \left(\boldsymbol{P}^{-1}(j\omega)\right)^{T} \quad \textbf{(51)}$$

where ⊗ denotes element-by-element multiplication (Schur product). Further information on how to interpret the RGA results and select pairings can be found at [10, 11].

The 6x6 (position and attitude) dynamic model of the Darwin-type spacecraft with large flimsy appendages has been analyzed by using the RGA method as a function of frequency and for the whole set of parameter uncertainty. Although the matrix obtained by means of (51) is a complex one, only the

absolute values are presented. By examining the corresponding matrices at each frequency, it is observed that the steady state results extend through low frequency up to 0.19 rad/sec. As a representative example within this range, (52) shows the results for the most coupled plant within the uncertainty at $\omega = 6.28 \cdot 10^{-4}$ rad/sec. According to it, the pairing should be done through the main diagonal of the matrix, which contains positive RGA elements, and the elements $g_{15}(s)$, $g_{24}(s)$, $g_{42}(s)$, $g_{51}(s)$ should also be considered relevant.

$$\boldsymbol{RGA}_{(\omega=6.28\cdot10^{-4}\,\text{rad/sec})} = \begin{bmatrix} \boldsymbol{1.0064} & 0 & 0 & 0 & \boldsymbol{0.0064} & 0 \\ 0 & \boldsymbol{1.0064} & 0 & \boldsymbol{0.0064} & 0 & 0 \\ 0 & 0 & \boldsymbol{1} & 0 & 0 & 0 \\ 0 & \boldsymbol{0.0064} & 0 & \boldsymbol{1.0064} & 0 & 0 \\ \boldsymbol{0.0064} & 0 & 0 & 0 & \boldsymbol{1.0064} & 0 \\ 0 & 0 & 0 & 0 & 0 & \boldsymbol{1} \end{bmatrix} \quad \textbf{(52)}$$

If the analysis is performed at high frequency, it produces the same concluding results in the entire spectrum starting at 3.51 rad/sec.

So far, the retained compensator elements would be those of the RGA matrix marked in bold in (52). Nevertheless, as aforementioned, the RGA elements increase and more interactions are founded in the interval of frequencies where the flexible modes of the satellite mostly affect (i.e. ω = [0.19-3.51] rad/sec), as can be seen in (53) and (54) for the most coupled plants at ω = 0.8 rad/sec and 1 rad/sec, respectively.

$$\boldsymbol{RGA}_{(\omega=0.8\,\text{rad/sec})} = \begin{bmatrix} \boldsymbol{1.1674} & 0.0001 & 0.0000 & 0.0012 & 0.3720 & 0.0001 \\ 0.0001 & \boldsymbol{1.0180} & 0.0000 & 0.0305 & 0.0013 & 0.0004 \\ 0.0000 & 0.0000 & \boldsymbol{4.8592} & 0.3468 & \boldsymbol{4.1456} & 0.0000 \\ 0.0012 & 0.0305 & 0.3468 & \boldsymbol{3.2030} & \boldsymbol{2.3865} & 0.0006 \\ 0.3720 & 0.0013 & \boldsymbol{4.1456} & \boldsymbol{2.3865} & \boldsymbol{7.2470} & 0.0008 \\ 0.0001 & 0.0004 & 0.0000 & 0.0006 & 0.0008 & \boldsymbol{1.0009} \end{bmatrix} \quad \textbf{(53)}$$

$$\boldsymbol{RGA}_{(\omega=1\,\text{rad/sec})} = \begin{bmatrix} \boldsymbol{0.9899} & 0.0002 & 0.0000 & 0.0001 & 0.0003 & 0.0102 \\ 0.0002 & \boldsymbol{0.9082} & 0.0000 & 0.0050 & 0.0009 & 0.0963 \\ 0.0000 & 0.0000 & \boldsymbol{3.1307} & \boldsymbol{2.3373} & 0.1110 & 0.0000 \\ 0.0001 & 0.0050 & \boldsymbol{2.3373} & \boldsymbol{12.5674} & \boldsymbol{9.4613} & 0.0690 \\ 0.0003 & 0.0009 & 0.1110 & \boldsymbol{9.4613} & \boldsymbol{10.2042} & 0.0302 \\ 0.0102 & 0.0963 & 0.0000 & 0.0690 & 0.0302 & \boldsymbol{0.7970} \end{bmatrix} \quad \textbf{(54)}$$

3.3.2 Controller Structure

In accordance with the above RGA results and taking into account the requirement of minimum controller complexity and order (Table IV), a first compensator structure consisting of six diagonal elements and four off-diagonal elements is chosen as the most suitable one (55).

$$\boldsymbol{G}(s) = \begin{bmatrix} g_{11}(s) & 0 & 0 & 0 & g_{15}(s) & 0 \\ 0 & g_{22}(s) & 0 & g_{24}(s) & 0 & 0 \\ 0 & 0 & g_{33}(s) & 0 & 0 & 0 \\ 0 & g_{42}(s) & 0 & g_{44}(s) & 0 & 0 \\ g_{51}(s) & 0 & 0 & 0 & g_{55}(s) & 0 \\ 0 & 0 & 0 & 0 & 0 & g_{66}(s) \end{bmatrix} \quad \textbf{(55)}$$

From this, four independent compensator design problems have been adopted, two SISO and two 2x2 MIMO problems: $[g_{33}(s)]$ and $[g_{66}(s)]$; $[g_{11}(s) \;\; g_{15}(s)\; ;\; g_{51}(s) \;\; g_{55}(s)]$ and $[g_{22}(s) \;\; g_{24}(s)\; ;\; g_{42}(s) \;\; g_{44}(s)]$, respectively. The SISO problems will be considered from the classical SISO QFT point of view, while the two 2x2 MIMO subsystems will be studied through the non-diagonal MIMO QFT methodology. The coupling detected in the range of frequencies of the flexible modes will be considered in the course of the design procedure through more demanding specifications with respect to disturbance rejection. Provided the performance results were not satisfactory, then the compensator structure should be filled up with additional off-diagonal compensators consistent with (53) and (54): g_{34}, g_{35}, g_{43}, g_{45}, g_{53} and g_{54} elements.

3.3.3 Robust Closed-Loop Specifications

The applied non-diagonal and diagonal MIMO QFT techniques design each loop individually, including the multivariable characteristic by means of their corresponding equivalent plant. So, the robust closed-loop specifications are defined in terms of SISO expressions for both SISO and MIMO subsystems.

Since these methodologies are frequency domain techniques, there is obviously a need for translating time domain requirements (Table IV) into the frequency domain. The original specifications in Table IV impose maximum and standard deviation values on the position and attitude time error signals, as well as actuator forces and torques. Their translation into the frequency domain is based on control-ratio models [9], and takes into account the expected external disturbances on the Darwin-type flyer, the spacecraft flexible modes and the coupling among loops. As a result, four Type of specifications are defined to calculate the QFT bounds: Type 1: Robust stability; Type 2: Robust sensitivity; Type 3: Robust disturbance rejection at plant input; and Type 4: Robust control effort attenuation.

The notation used for the signals in the following description of specifications refers to the scheme of the generic MIMO subsystem presented in Fig. 12. The compensators have been designed within the set of frequencies of interest $\omega = [6.28 \cdot 10^{-4}, 62.8]$ rad/sec.

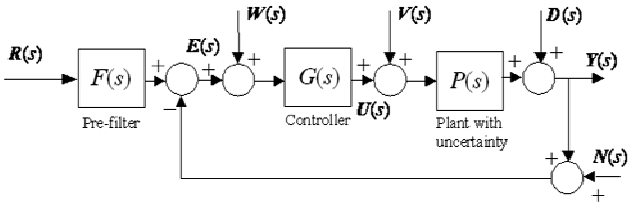

Fig. 12 Structure of a 2 Degree of Freedom MIMO System

Type 1: Robust Stability specification

This specification, shown in (56), is stated to guarantee a robust stable control. All the required values, displayed loop by loop in (57) and (58), imply at least 1.54 (3.75 dB) gain margin and at least 49.25º phase margin. The specification corresponds not only to the closed-loop transfer function $y_i(s)/r_i(s)$, but also to transfer functions $y_i(s)/n_i(s)$ and $u_i(s)/v_i(s)$. Hence this condition additionally imposes the requirements on sensor noise attenuation, disturbance rejection at plant input and flexible modes.

$$\left| \frac{\left[p_{ii}^{*e}(s)\right]_i^{-1} g_{ii}(s)}{1+\left[p_{ii}^{*e}(s)\right]_i^{-1} g_{ii}(s)} \right| \le \delta_1(\omega) \qquad \textbf{(56)}$$

where $[p_{ii}^{*e}(s)]_i^{-1}$ is the inverse of the equivalent plant (45), which corresponds to $p_{ii}(s)$ in SISO designs.

Loops 1, 2 and 3: $\delta_1(\omega) = 1.85 \quad ; \ \forall\omega$ **(57)**

Loops 4, 5 and 6: $$\delta_1(\omega) = \left| \frac{0.1687}{s^2 + 0.4s + 0.0912} \right| \quad ; \ \forall\omega \qquad \textbf{(58)}$$

Type 2: Sensitivity reduction

The main objective of this specification, (59) and (60), is sensor noise attenuation and reduction of the effect of the parameter uncertainty on the closed-loop transfer function. It corresponds to $e_i(s)/n_i(s)$ and $[dt_{ii}(s)/t_{ii}(s)] / [dp_{ii}(s)/p_{ii}(s)]$ transfer functions.

$$\left| \frac{1}{1 + \left[p_{ii}^{*e}(s) \right]_i^{-1} g_{ii}(s)} \right| \le \delta_2(\omega) \qquad \textbf{(59)}$$

All loops: $\delta_2(\omega) = 2 \quad ; \ \forall\omega$ **(60)**

Type 3: Rejection of disturbances at plant input

Solar pressure perturbation and gravity gradient are considered to affect at plant input in the form of both force and torque. The purpose of this specification (61), which corresponds to $e_i(s)/v_i(s)$ and $y_i(s)/v_i(s)$ transfer functions, is to attenuate the effect of plant input disturbances on the control error and the output signal. Thus, a high gain is required in the low frequency band, (62) to (64). Besides, since $v_i(s)$ also represents the flexible modes, special attention is paid to their frequency range mainly to accomplish the attitude requirements.

$$\left| \frac{\left[p_{ii}^{*e}(s) \right]_i^{-1}}{1 + \left[p_{ii}^{*e}(s) \right]_i^{-1} g_{ii}(s)} \right| \le \delta_3(\omega) \qquad \textbf{(61)}$$

Loops 1 and 2: $$\delta_3(\omega) = \left| \frac{0.21553\,(s + 0.385)}{(s + 0.307)(s + 6.18)(s^2 + 0.4s + 0.0912)} \right| \quad ; \ \forall\omega \qquad \textbf{(62)}$$

Loop 3: $$\delta_3(\omega) = \left| \frac{0.313\,(s - 0.01705)(s^2 + 0.009974s + 5.104 \cdot 10^{-5})}{(s - 0.01813)(s^2 + 0.02554s + 0.0004754)} \right| \quad ; \ \forall\omega \qquad \textbf{(63)}$$

Loops 4, 5 and 6:

$$\delta_3(\omega) = \left| \frac{(s + 0.2)(s + 0.186)(s + 0.2044)(s + 0.003892)(s^2 + 0.06014s + 0.02736)}{(s + 0.007333)(s + 0.445)(s^2 + 0.07904s + 0.00326)(s^2 + 0.2352s + 0.0981)} \right| \quad ; \ \forall\omega \qquad \textbf{(64)}$$

Type 4: Control signal

Because of saturation limits, control signal movements should be kept reasonably small despite disturbances coming from actuators and sensors. This specification, (65), corresponds to $u_i(s)/n_i(s)$ transfer function and is depicted in (66)-(68).

$$\left| \frac{g_{ii}(s)}{1 + \left[p_{ii}^{*e}(s) \right]_i^{-1} g_{ii}(s)} \right| \le \delta_4(\omega) \qquad \textbf{(65)}$$

$$\text{Loops 1 and 2:}\quad \delta_4(\omega)=\left|\frac{557.1\,(s+5)}{(s^2+3.23s+6.5)}\right| \quad ;\quad \forall\omega \tag{66}$$

$$\text{Loop 3:}\quad \delta_4(\omega)=\left|\frac{106.9210\,(s+0.55)(s^2+0.04s+0.13)}{(s+1.4)^2\,(s^2+0.1227s+0.097)}\right| \quad ;\quad \forall\omega \tag{67}$$

$$\text{Loops 4, 5 and 6:}\quad \delta_4(\omega)=\left|\frac{4.026\,(s^2-0.1854s+0.203)(s^2+0.04s+0.504)}{(s^2+0.305s+0.056)(s^2+0.115s+0.095)}\right| \quad ;\quad \forall\omega \tag{68}$$

Reducing coupling effects as much as possible

The coupling effects from other axes can be considered as part of the disturbances acting at the input of the equivalent SISO plant. The way of designing the non-diagonal elements of the matrix compensator deals with the aim of minimizing the off-diagonal elements of the coupling matrix (32).

3.3.4 SISO Design Problems: $g_{33}(s)$, $g_{66}(s)$

Compensators $g_{33}(s)$ and $g_{66}(s)$ are independently designed by using classical SISO QFT [1] to satisfy the robust stability and robust performance specifications stated in Section 3.3.3 for every plant within the set of uncertain plants. The corresponding QFT bounds and the nominal case of the designed open-loop transfer functions $L_{ii}(s) = p_{ii}(s)\, g_{ii}(s)$, i = 3, 6, are plotted on the Nichols Chart for some of the most relevant frequencies in Fig. 13(a) and 13(b) for loops 3 and 6 respectively. Both designs satisfy not only their respective bounds but also the Nyquist encirclement condition, and no RHP pole-zero cancellations occur between $g_{33}(s)$ and $p_{33}(s)$, nor between $g_{66}(s)$ and $p_{66}(s)$. The Bode plot of each compensator can be found in Section 3.6, where $g_{33}(s)$ [Fig. 18(a)] and $g_{66}(s)$ [Fig. 18(b)] are represented in solid line in comparison with the H-infinity design (dashed line) introduced in Section 3.5. The QFT compensator expressions are presented in Section 3.5.

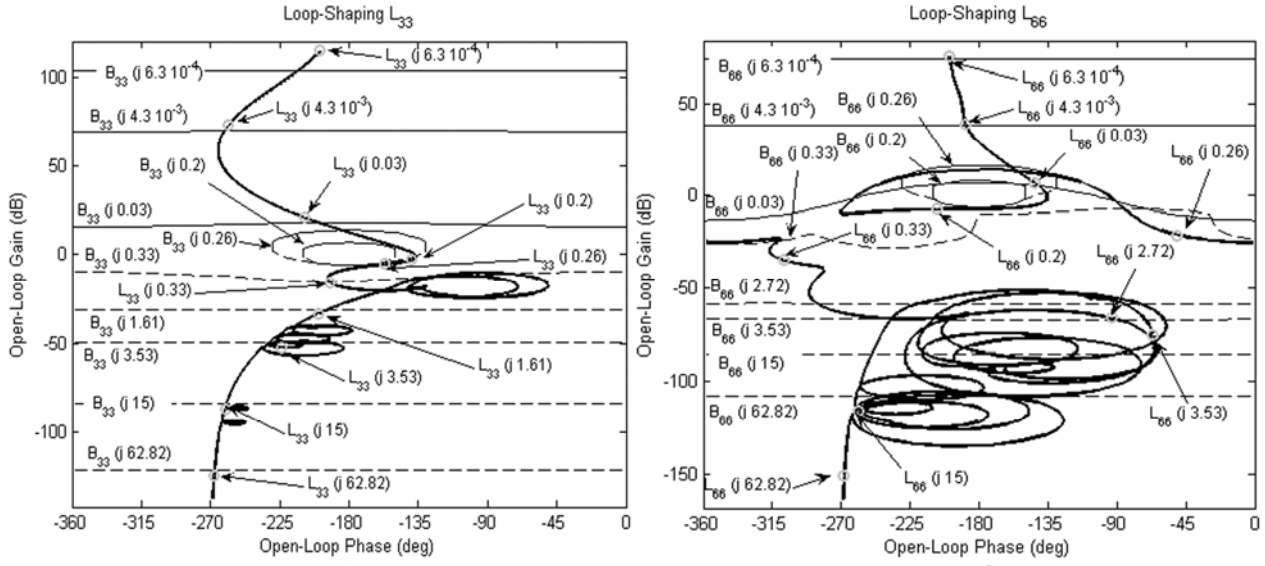

(a) (b)

Fig. 13 Loop-shaping (a) $L_{33}(s) = p_{33}(s)\, g_{33}(s)$. (b) $L_{66}(s) = p_{66}(s)\, g_{66}(s)$

3.3.4.1 First MIMO Problem: $g_{11}(s)$, $g_{51}(s)$, $g_{55}(s)$, $g_{15}(s)$ Design

The compensator for this 2x2 MIMO problem has been designed by applying the non-diagonal MIMO QFT methodology developed by Garcia-Sanz *et al*. [1-7] and outlined in Section 2. In this particular case, the plant to be controlled is composed of the following elements coming from the original 6x6 Darwin-type spacecraft model $\boldsymbol{P}^{15}(s) = [p_{11}(s) \;\; p_{15}(s) \; ; \; p_{51}(s) \;\; p_{55}(s)]$, whose inverse matrix is $\boldsymbol{P}^{15*}(s) = [\boldsymbol{P}^{15}(s)]^{-1} = [p_{11}^{*}(s) \;\; p_{15}^{*}(s) \; ; \; p_{51}^{*}(s) \;\; p_{55}^{*}(s)]$.

Step A: Arrangement of the system

First, the methodology adopts the structure and the pairing of inputs and outputs given by the RGA technique in (55) and arranges the plant inverse matrix $\boldsymbol{P}^{15*}(s)$ so that the inverse of the first diagonal element in this matrix has the smallest phase margin frequency [1]. In some cases, arbitrarily picking the wrong order of the loops could lead to the non-existence of a solution. In the present problem, the bandwidth of the loops is quite similar. Then, any order can be selected to design the non-diagonal MIMO QFT compensators.

Step B1: Design of the diagonal compensator $g_{11}(s)$

The diagonal compensator $g_{11}(s)$ is designed through standard QFT loop-shaping [1] for the inverse of the equivalent plant $[p_{11}^{*e}(s)]_1 = p_{11}^{*}(s)$ to fulfill the robust stability and robust performance specifications determined in Section 3.3.3 for every plant within the set of uncertain plants. Fig. 14(a) shows the nominal case of the designed open-loop transfer function $L_{11}(s) = [p_{11}^{*e}(s)]_1^{-1} \; g_{11}(s)$ in bold solid line, which satisfies the QFT bounds, also represented in the figure. Additionally, the design fulfils the first two sufficient stability conditions (c.1) and (c.2) (Section 2.6). That is, $L_{11}(s) = [p_{11}^{*e}(s)]_1^{-1} \; g_{11}(s)$ satisfies the Nyquist encirclement condition and no RHP pole-zero cancellations occur between $g_{11}(s)$ and $[p_{11}^{*e}(s)]_1^{-1}$. The Bode plot for the obtained compensator $g_{11}(s)$ is presented in Fig. 19(a) (solid line) together with the design of the H-infinity approach.

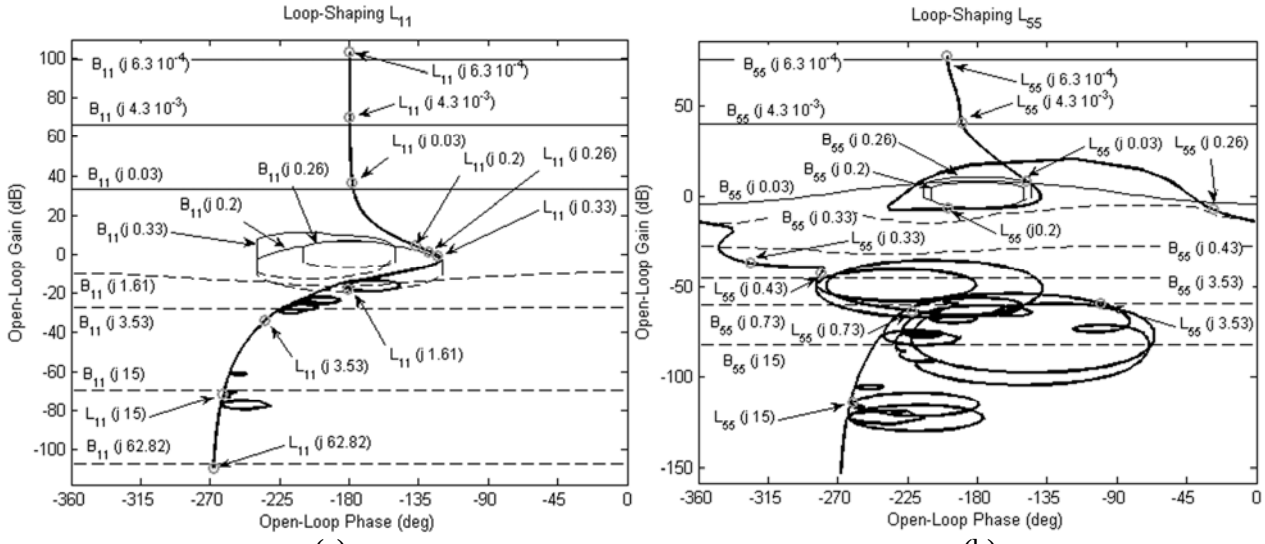

Fig. 14 Loop-shaping (a) $L_{11}(s) = [p_{11}^{*e}(s)]_1^{-1} \; g_{11}(s)$. (b) $L_{55}(s) = [p_{55}^{*e}(s)]_2^{-1} \; g_{55}(s)$

Step C$_1$: Design of the non-diagonal compensator $g_{51}(s)$

The non-diagonal compensator $g_{51}(s)$ is designed to minimize the (5,1) element of the coupling matrix in the case of disturbance rejection at plant input (32), which gives the following expression:

$$g_{51}^{opt}(s) = -\,p_{51}^{*\,N}(s) \tag{69}$$

where N denotes the plant that minimizes the maximum of the non-parametric uncertainty radii comprising the plant templates on the Nichols Chart. Due to the uncertainty, the expression $[-p_{51}^{*}(s)]$ determines a region in the magnitude and phase plots, where the compensator $g_{51}(s)$ is shaped following the mean value at every frequency $\omega \in [0, 0.1]$ rad/sec [see Fig. 15 with $g_{51}(s)$ interpolating the plot]. The compensator Bode plot is compared in Fig. 19(c) with that of the (5,1) element of the H-infinity compensator introduced in Section 3.5.

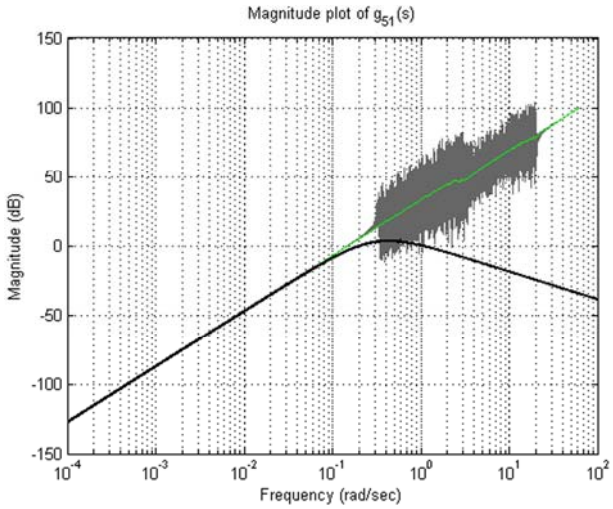

Fig. 15 Magnitude plot of $[-p_{51}^{*}(s)]$ with uncertainty and $g_{51}(s)$ –bold solid line-

Step B_2: Design of the diagonal compensator $g_{55}(s)$

As in step B_1, the diagonal compensator $g_{55}(s)$ is designed to control the inverse of the equivalent plant, $[p_{55}^{*e}(s)]_2^{-1}$, which takes the compensator previously designed into account (45).

$$\left[p_{55}^{*e}(s)\right]_2 = \left[p_{55}^{*e}(s)\right]_1 - \frac{\left(\left[p_{51}^{*e}(s)\right]_1 + \left[g_{51}(s)\right]_1\right)\left(\left[p_{15}^{*e}(s)\right]_1\right)}{\left[p_{11}^{*e}(s)\right]_1 + \left[g_{11}(s)\right]_1} \tag{70}$$

On the basis of the robust specifications defined in Section 3.3.3 for $[p_{55}^{*e}(s)]_2^{-1}$, and also taking into account the plant uncertainty, the QFT bounds are computed. Then, the compensator is designed by classical loop-shaping on the Nichols Chart, as is shown in Fig. 14(b). Not only does the design fulfil the bounds but also the first two stability conditions of (c.1) and (c.2) from Section 2.6. In other words, $L_{55}(s) = [p_{55}^{*e}(s)]_2^{-1}\, g_{55}(s)$ satisfies the Nyquist encirclement condition and no RHP pole-zero cancellations occur between $g_{55}(s)$ and $[p_{55}^{*e}(s)]_2^{-1}$. The Bode plot of $g_{55}(s)$ is presented in Fig. 19(d).

Step C_2: Design of the non-diagonal compensator $g_{15}(s)$

Due to the requirement of minimum controller complexity and order (Table IV), the non-diagonal compensator $g_{15}(s)$ has been set to zero. Anyway, the equivalent expression to the one used in (69), $g_{15}^{opt}(s) = -p_{15}^{*N}(s)$, could be applied to cancel interaction in both directions in the MIMO subsystem.

At this point, once the whole controller of the MIMO subsystem has been determined, the last two stability conditions mentioned in Section 2.6, (c.3) and (c.4), are checked. The system is stable. Finally,

the non-existence of RHP transmission zeros of $\boldsymbol{P}(s)\,\boldsymbol{G}(s)$ is checked by using the Smith-McMillan form over the set of possible plants $\Im\mathbf{P}$ due to uncertainty [5]. The non-diagonal MIMO QFT compensator expressions are presented in Section 3.6.

3.3.4.2 Second MIMO Problem: $g_{22}(s)$, $g_{42}(s)$, $g_{44}(s)$, $g_{24}(s)$ Design

The second MIMO problem consists of the following elements: $\boldsymbol{P}^{24}(s) = [p_{22}(s) \;\; p_{24}(s) \;;\; p_{42}(s) \;\; p_{44}(s)]$. From the 2x2 plant inverse matrix $\boldsymbol{P}^{24*}(s) = [\boldsymbol{P}^{24}(s)]^{-1} = [p_{22}^{*}(s) \;\; p_{24}^{*}(s) \;;\; p_{42}^{*}(s) \;\; p_{44}^{*}(s)]$ and taking into account the robust stability and robust performance specifications (Section 3.3.3), the non-diagonal MIMO QFT methodology is equivalently performed by following the steps detailed in Section 2.

The loop-shaping for the diagonal compensator elements $g_{22}(s)$ and $g_{44}(s)$ are shown in Fig. 16(a) and 16(b), respectively. The Bode plots for the four compensators are shown in Fig. 20(a), (b), (c) and (d) for $g_{22}(s)$, $g_{24}(s)$, $g_{42}(s)$, $g_{44}(s)$, respectively. The 2x2 MIMO subsystem is found to be stable according to the sufficient stability conditions (Section 2.6). Finally, it is also checked that no additional RHP zeros have been introduced by the compensator [5]. The non-diagonal MIMO QFT compensator expressions are presented in Section 3.6.

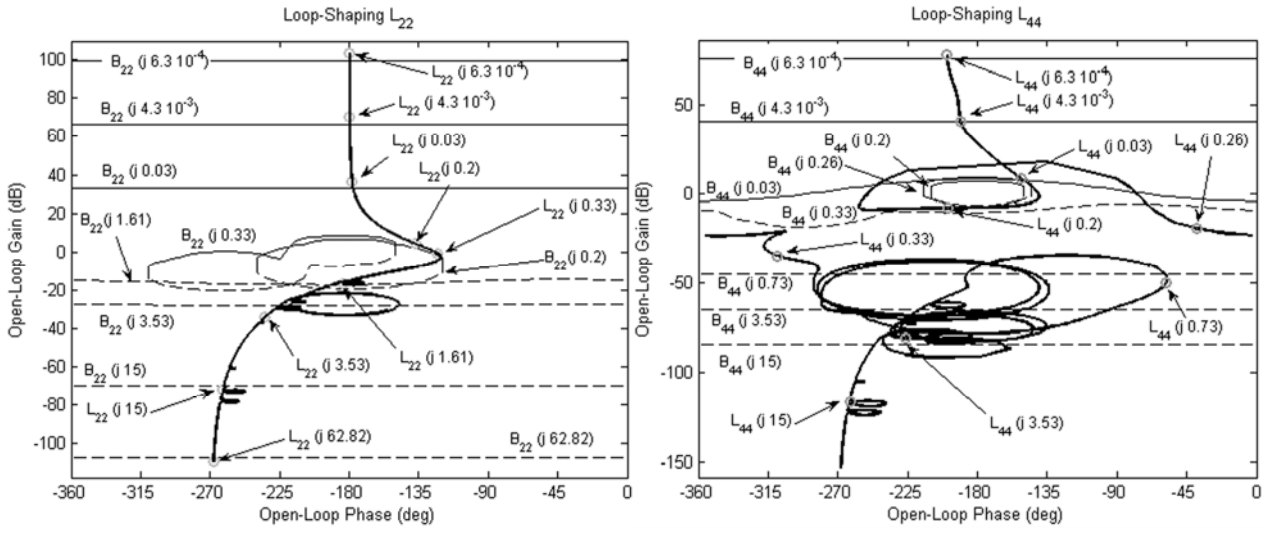

(a) (b)

Fig. 16 Loop-shaping (a) $L_{22}(s) = [p_{22}^{*e}(s)]_1^{-1}\, g_{22}(s)$. (b) $L_{44}(s) = [p_{44}^{*e}(s)]_2^{-1}\, g_{44}(s)$

3.4 Diagonal MIMO QFT Controller Design

For the sake of comparison, the sequential diagonal MIMO QFT methodology developed by Horowitz [12] is also applied to control the position and attitude of the Darwin-type Flyer. Based on the same robust closed-loop specifications defined in Section 3.3.3, this technique uses a sequential procedure similar to the one detailed in Section 2.5 (Step B), where the recursive expression of the equivalent plant is a simplified case of (45), with $g_{ij}(s) = 0$ $(i \neq j)$.

For the Darwin-type Flyer, the loop-shaping step of the diagonal method requires the same diagonal compensators $g_{ii}(s)$ as the non-diagonal one. This happens because, in this case, in the middle and high frequency range the off-diagonal elements $g_{ij}(s)$ $(i \neq j)$ of the non-diagonal controller have less relative influence than the corresponding $p_{ij}^{*}(s)$ elements in the equivalent plant (45). Differences between both MIMO QFT controllers arise in the low frequency range, as can be observed in Fig. 17. The $\boldsymbol{C}_2(5,1)$ element of the coupling matrix for disturbances at plant input (32) is plotted for a representative plant case

and for the three controllers: non-diagonal and diagonal MIMO QFT and H-infinity designs. For the frequency range $\omega \in [0, 0.1]$ rad/sec it is shown that $\boldsymbol{C}_2(5,1)_{\text{non-diag QFT}} < \boldsymbol{C}_2(5,1)_{\text{diag QFT}} < \boldsymbol{C}_2(5,1)_{\text{H-infinity}}$, which explains why the non-diagonal MIMO QFT improves the diagonal MIMO QFT and the H-infinity controller results under low frequency external disturbances (see Section 3.6.2).

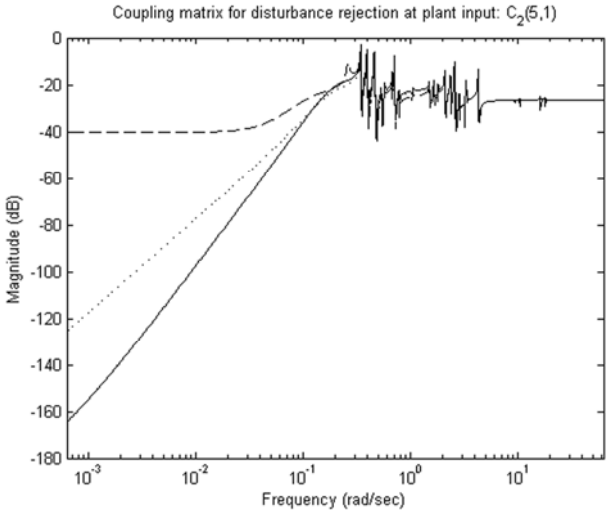

Fig. 17 Element (5,1) of the coupling matrix C_2: non-diagonal MIMO QFT in solid line, diagonal MIMO QFT in dotted line, H-infinity in dashed line

3.5 Controllers

The notation adopted for transfer function expressions denotes the steady state gain as a constant without parenthesis; simple poles and zeros as (ω), which corresponds to (s/ω + 1) denominator and numerator, respectively; poles and zeros at the origin as (0); conjugate poles and zeros as [ξ ; ω_n], with $((s/\omega_n)^2 + (2\xi/\omega_n)\, s + 1)$ denominator and numerator, each; *n*-multiplicity of poles and zeros as an exponent $(\,)^n$.

The non-diagonal MIMO QFT compensator consists of the following eight elements: $g_{11}(s) = g_{22}(s) =$ {31.5 (0.6194) (0.2138) (0.1663) (0.1649)} / {(0.666) (0.4982) (0.07526) [0.676; 1.479]} ; $g_{51}(s) = -g_{42}(s) =$ {42.4 $(0)^2$ } / {$(0.3)^3$}; $g_{15}(s) = g_{24}(s) = 0$; $g_{33}(s) =$ {125 (0.13) (0.057) [0.07019; 0.3565] [1; 0.02]} / {(1.48) (0.7875) (0.2) (0.004) (0.00246) [0.18; 0.314]}; $g_{44}(s) =$ {2.242 (0.03412) [0.08644; 0.7114] [0.1131; 0.3414] [0.1145; 0.2604] [0.008792; 0.2593] [0.7; 0.0052] [1; 0.0007]} / {(0.9776) (0.8) $(0.0005)^2$ [0.2451; 0.2708] [0.297; 0.2673] [-0.0005; 0.254] [0.14; 0.252] [0.7; 0.0045]}; $g_{55}(s) =$ {2.242 (0.13) (0.03) [0.1079; 0.7099] [0.07069; 0.341] [0.03; 0.2593] [0.7; 0.0052] [1; 0.0007]} / {(0.9776) (0.8) (0.12) $(0.0005)^2$ [0.2451; 0.2708] [-0.0008; 0.254] [0.3; 0.25] [0.7; 0.0045]}; $g_{66}(s) =$ {2.242 (0.02584) [0.08644; 0.7114] [0.1131; 0.3414] [0.1145; 0.2604] [0.008792; 0.2593] [0.7; 0.0052] [1; 0.0007]} / {(0.9776) (0.8) $(0.0005)^2$ [0.2451; 0.2708] [0.297; 0.2673] [-0.0007; 0.254] [0.1687; 0.241] [0.7; 0.0045]}.

The diagonal MIMO QFT compensator consists of the same diagonal elements $g_{ii}(s)$ as the non-diagonal compensator abovementioned, and $g_{ij}(s) = 0$, $i \neq j$.

The main elements of the 1-DOF H-infinity compensator are shown in Figs. 18-20. Their dc gains stay within the range [-15 dB, 26 dB]. The remaining 26 elements present a very low gain, going from -260 dB to -330 dB.

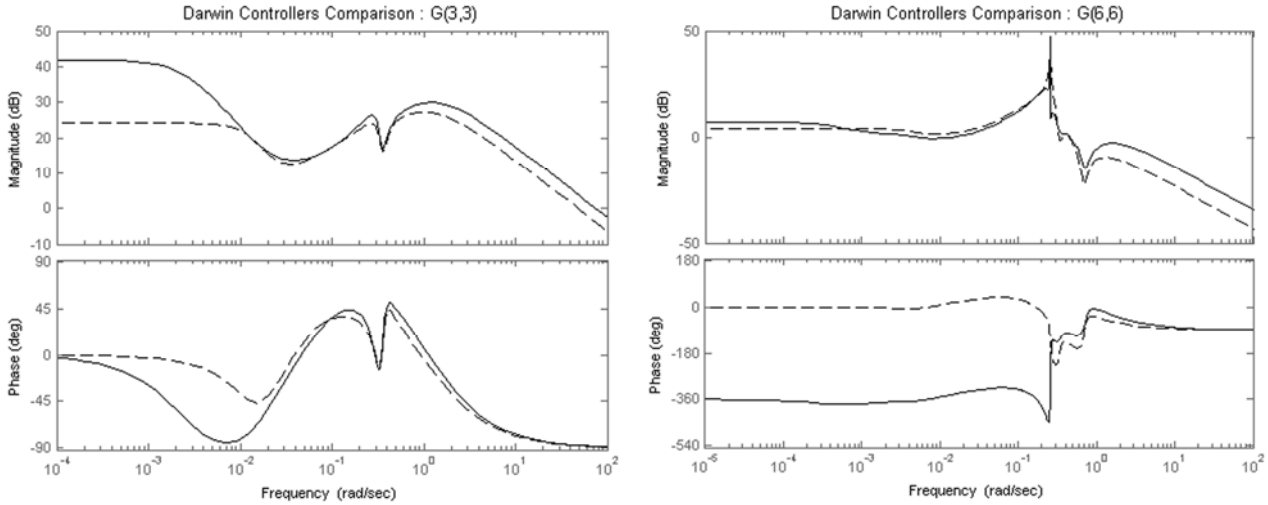

(a) (b)

Fig. 18 Bode Diagram Compensators: non-diagonal and diagonal MIMO QFT in solid line, H-infinity in dashed line. (a) $g_{33}(s)$, (b) $g_{66}(s)$

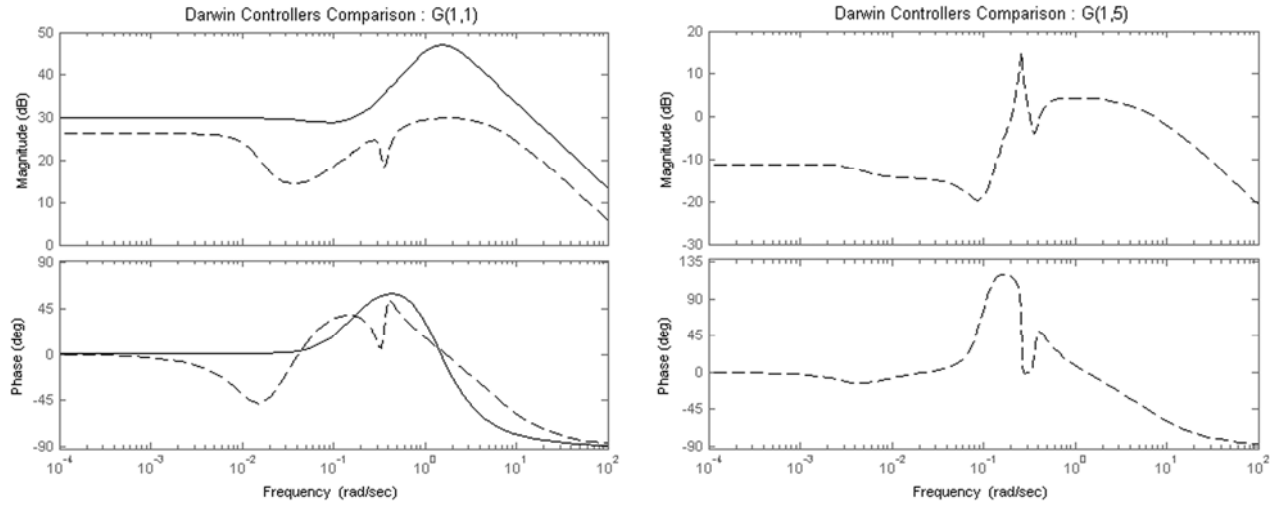

(a) (b)

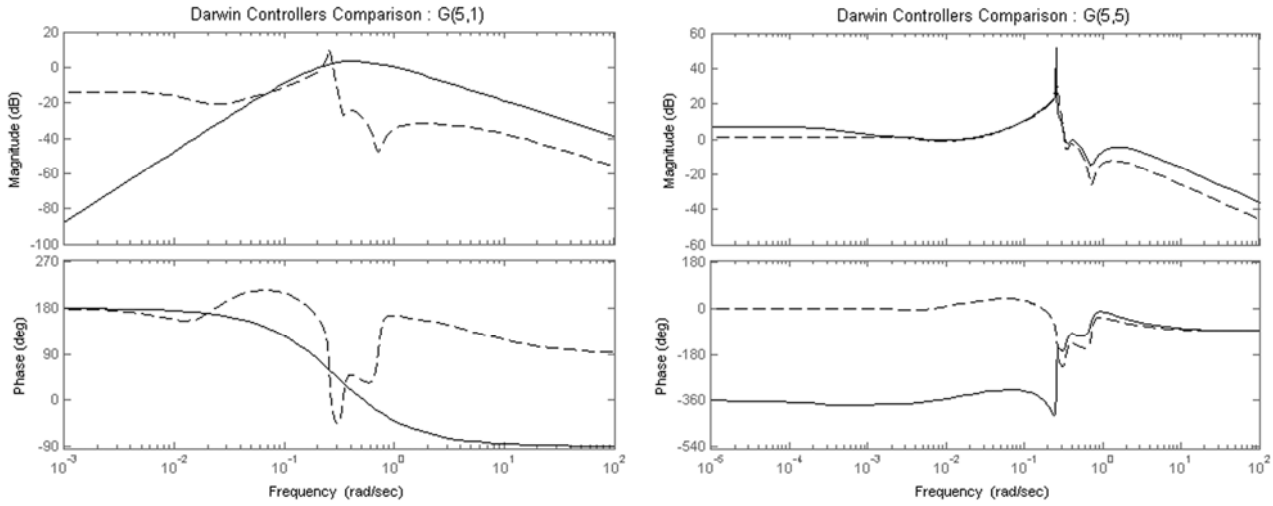

(c) (d)

Fig. 19 Bode Diagram Compensators: non-diagonal MIMO QFT in solid line [also diagonal MIMO QFT for $g_{11}(s)$ and $g_{55}(s)$], H-infinity in dashed line. (a) $g_{11}(s)$, (b) $g_{15}(s)$, (c) $g_{51}(s)$, (d) $g_{55}(s)$

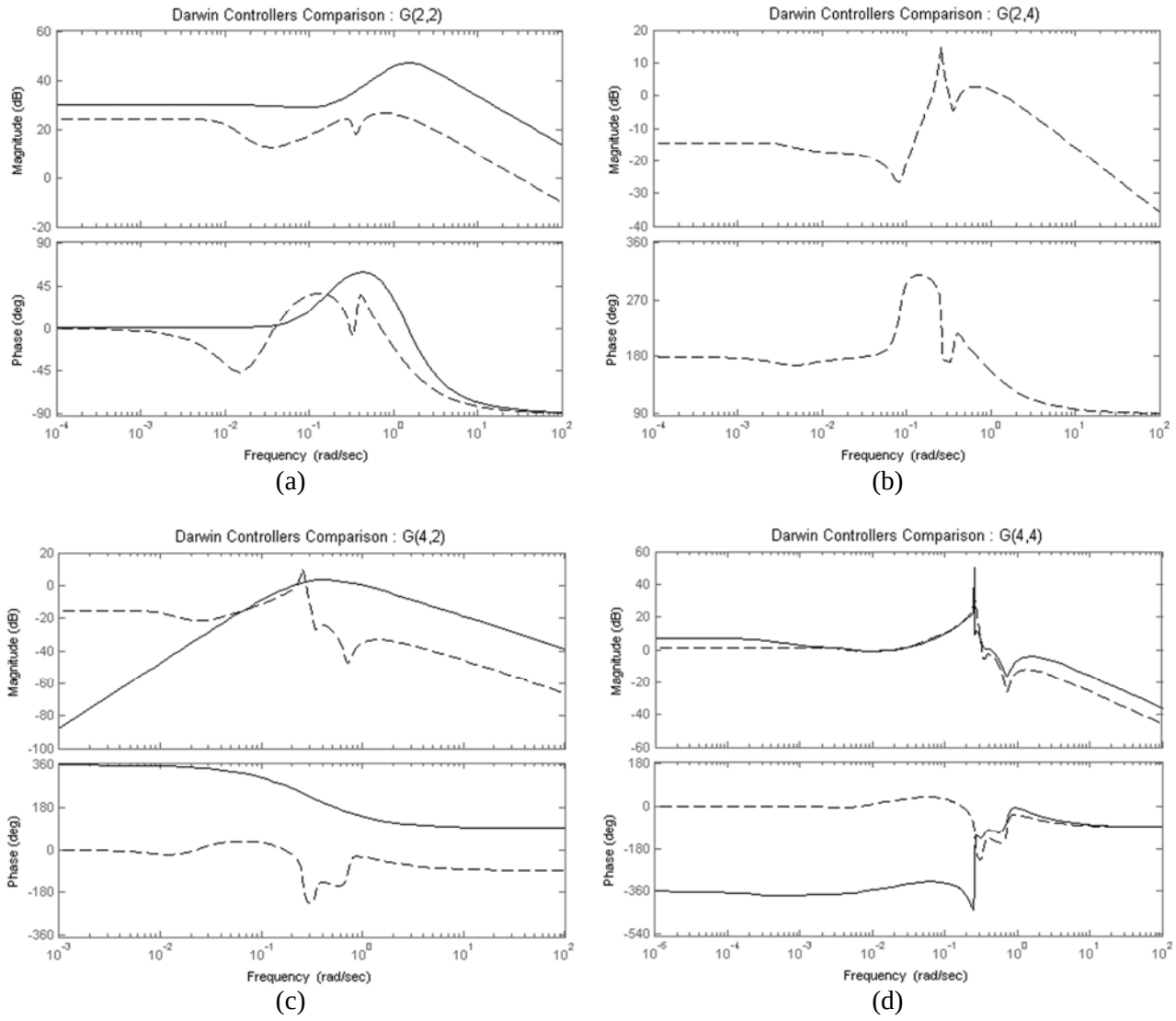

Fig. 20 Bode Diagram Compensators: non-diagonal MIMO QFT in solid line [also diagonal MIMO QFT for $g_{22}(s)$ and $g_{44}(s)$], H-infinity in dashed line. (a) $g_{22}(s)$, (b) $g_{24}(s)$, (c) $g_{42}(s)$, (d) $g_{44}(s)$

3.6 Comparative evaluation

This section shows a comparative analysis of the sequential non-diagonal MIMO QFT controller, designed above for the 6x6 Darwin-type Flyer, with both sequential diagonal MIMO QFT and H-infinity controllers. First, comparative Bode plots of the compensators are shown. Then, time performance results are presented (astronomical requirements), followed by open-loop bandwidth, and forces and torques comparison (engineering requirements). Finally, the stability objectives and the order of each compensator are analyzed (control requirements).

3.6.1 Compensators Bode Plots

The Bode plots are presented for the compensators of the non-diagonal MIMO QFT (solid line) in comparison with those of the H-infinity (dashed line). Note that, in this case, the diagonal MIMO QFT method yields the same diagonal compensators as the non-diagonal MIMO QFT technique. Fig. 18 presents the results for the two SISO subsystems $g_{33}(s)$ and $g_{66}(s)$, (a) and (b) respectively. Fig. 19 plots

the compensators of the 2x2 MIMO subsystem composed of $g_{11}(s)$, $g_{15}(s)$, $g_{51}(s)$ and $g_{55}(s)$ elements. The $g_{22}(s)$, $g_{24}(s)$, $g_{42}(s)$ and $g_{44}(s)$ compensator elements that conform the other 2x2 MIMO subsystem are shown in Fig. 20. Note that $g_{15}(s)$ and $g_{24}(s)$ have been set to zero in the non-diagonal MIMO QFT design. Additionally, according to the RGA results in (55) the remaining elements of the controller matrix $\boldsymbol{G}(s)$ designed with this technique equal zero. By contrast, those 26 elements present a non-zero, although very small, magnitude response when they are designed with the H-infinity technique. Finally, the off-diagonal elements of the diagonal MIMO QFT are obviously zero.

Table V. Time simulation performance with the three controllers

	Specification	Requirement	Benchmark	Non-diagonal MIMO QFT Controller	Diagonal MIMO QFT Controller	H-infinity Controller
1	Maximum Position Error X (μm)	< 1 μm	B1 B2	**0.0131** **0.0816**	**0.0131** **0.0816**	0.0293 0.511
2	Maximum Position Error Y (μm)	< 1 μm	B1 B2	**0.0120** **0.0120**	**0.0120** **0.0120**	0.0299 0.0299
3	Maximum Position Error Z (μm)	< 1 μm	B1 B2	**0.0288** **0.0288**	**0.0288** **0.0288**	0.0292 0.0292
4	Maximum Attitude Error X (mas)	< 25.5 mas	B1 B2	**25.27** **25.27**	25.31 25.31	25.95 25.95
5	Maximum Attitude Error Y (mas)	< 25.5 mas	B1 B2	**22.91** **22.55**	22.99 23.75	23.21 28.91
6	Maximum Attitude Error Z (mas)	< 25.5 mas	B1 B2	**21.15** **21.15**	**21.15** **21.15**	22.84 22.84
7	Std. Deviation of Position Error X (μm)	< 0.33 μm	B1 B2	**0.00275** **0.0511**	0.00276 **0.0511**	0.00686 0.341
8	Std. Deviation of Position Error Y (μm)	< 0.33 μm	B1 B2	**0.00265** **0.00265**	0.00266 0.00266	0.00722 0.00722
9	Std. Deviation of Position Error Z (μm)	< 0.33 μm	B1 B2	**0.00668** **0.00668**	**0.00668** **0.00668**	0.00691 0.00691
10	Std. Deviation of Attitude Error X (mas)	< 8.5 mas	B1 B2	**5.57** **5.57**	**5.57** **5.57**	5.68 5.68
11	Std. Deviation of Attitude Error Y (mas)	< 8.5 mas	B1 B2	**5.76** **5.80**	**5.76** 5.85	6.01 8.23
12	Std. Deviation of Attitude Error Z (mas)	< 8.5 mas	B1 B2	**4.83** **4.83**	**4.83** **4.83**	5.00 5.00
13	Maximum Actuator Force Command X (N)	< 1.5e-4 N	B1 B2	1.94e-6 3.94e-6	1.94e-6 3.94e-6	**7.42e-7** **3.31e-6**
14	Maximum Actuator Force Command Y (N)	< 1.5e-4 N	B1 B2	1.86e-6 1.86e-6	1.86e-6 1.86e-6	**6.68e-7** **6.68e-7**
15	Maximum Actuator Force Command Z (N)	< 1.5e-4 N	B1 B2	5.94e-7 5.94e-7	5.94e-7 5.94e-7	**5.61e-7** **5.61e-7**
16	Maximum Actuator Torque Command X (Nm)	< 1.5e-4 N m	B1 B2	**8.68e-7** **8.68e-7**	8.71e-7 8.71e-7	1.03e-6 1.03e-6
17	Maximum Actuator Torque Command Y (Nm)	< 1.5e-4 N m	B1 B2	**1.05e-6** **1.06e-6**	**1.05e-6** **1.06e-6**	1.15e-6 1.16e-6
18	Maximum Actuator Torque Command Z (Nm)	< 1.5e-4 N m	B1 B2	**1.08e-6** **1.08e-6**	**1.08e-6** **1.08e-6**	1.27e-6 1.27e-6

3.6.2 Astronomical Requirements

Time simulations are performed for 300 random dynamics within the uncertainty range (MonteCarlo analysis) in the original ESA benchmark simulator (B1) described in Section 3.1 and in a complementary benchmark (B2), both developed under Matlab/Simulink. The latter just adds to B1 a low frequency disturbance force at plant input along the X-axis (magnitude: 2 μN, frequency: $\omega = 0.05$ rad/sec) in order to consider disturbance rejection and coupling attenuation at low frequencies. In each simulation, the criteria appearing in Table IV are computed over the entire simulation time (i.e. 5000 sec).
In order to characterize the minimum performance obtained, the worst results reached by every controller are presented in Table V. In other words, for each controller, the greatest value over the 300 uncertain cases is shown for the maximum and the standard deviation of position and attitude errors, as well as for maximum actuator commands, in all axes. Then, it is possible to verify whether the worst performance still respects the requirement. The bold number in every row of Table V represents the best result (best control strategy) for every particular specification.

Position errors (1,2,3,7,8,9 –Table V)

By inspecting Table V, it is found that the performance obtained in time simulations is very good concerning position accuracy, since the requirements are easily fulfilled (an improvement of two orders of magnitude with respect to the specification is achieved in benchmark B1, and at least one order of magnitude in benchmark B2) for maximum and standard deviation values. The non-diagonal MIMO QFT design either equals or slightly improves the diagonal MIMO QFT. Both QFT controllers improve the H-infinity results for the two benchmarks.

Attitude errors (4,5,6,10,11,12 –Table V)

The specification for the highest attitude error is harder to meet mainly because of the effect of the flexible modes. Some of the maximum attitude values of the H-infinity even exceed the 25.5 mas required: see benchmark B1 (4 –Table V) and benchmark B2 (4,5 –Table V). Again, the MIMO QFT methodologies improve the results of the H-infinity controller in the six attitude error cases (4,5,6,10,11,12 –Table V).

Once more, the non-diagonal MIMO QFT either equals or improves the diagonal QFT controller results. The greatest differences between both controllers can be observed at the Attitude Error along the Y-axis (5,11 –Table V), especially for benchmark B2. There, the non-diagonal design decreases the standard deviation attitude error by 0.85 % (11 –Table V) and the maximum attitude error by 5.05 % (5 –Table V) with respect to the values reached by the diagonal compensator. These improvements could turn out to be relevant to the astronomical mission. Their achievement is due to the fact that the off-diagonal compensators have been designed to minimize the coupling at low frequencies, which are principally stressed in the second benchmark.

3.6.3 Engineering Requirements

Saturation limits. Actuator commands (13,14,15,16,17,18 –Table V)

As can be seen in Table V, actuation is very small and far below the saturation limits. The results for the three controllers remain at similar values (13,14,15,16,17,18 –Table V).

Open-loop Bandwidth Comparison

The open-loop cross-over frequency results of the six SISO loop subsystems are shown in Table VI. These measures correspond to the smallest frequencies in Hz where the transfer functions of the open-loop of each SISO subsystem $p_{ii}(s)$ $g_{ii}(s)$ [without the coupling elements $p_{ij}(s)$, $i \neq j$] are equal to 0 dB. The

minimum performance for each of the three designs has been established as the minimum bandwidth value over the 300 random satellite dynamics. Obviously, the bandwidth results for the two MIMO QFT designs coincide since their diagonal compensators are the same. A value of 0.01 Hz is considered a good compromise choice for bandwidth. Since the frequencies of the first flexible modes are within the range [0.05, 0.5] Hz, the open-loop cross-over frequencies for attitude and position are tuned to be as high as possible while simultaneously preventing the flexible modes from disturbing the system output performance.

Table VI. Frequency performance with the three controllers

	Requirement	Non-diagonal MIMO QFT Controller	Diagonal MIMO QFT Controller	H-infinity Controller
Position Bandwidth X (Hz)	0.01 Hz	0.0464	0.0464	0.0229
Position Bandwidth Y (Hz)	0.01 Hz	0.0472	0.0472	0.0206
Position Bandwidth Z (Hz)	0.01 Hz	0.0212	0.0212	0.0205
Attitude Bandwidth X (Hz)	0.01 Hz	0.00949	0.00949	0.0102
Attitude Bandwidth Y (Hz)	0.01 Hz	0.0102	0.0102	0.0102
Attitude Bandwidth Z (Hz)	0.01 Hz	0.00883	0.00883	0.0102
$\max_{\omega}\lvert \boldsymbol{T}(j\omega)\rvert$ **(dB)**	<6 dB	12.73 (Max) 5.64 (Mean)	11.51 (Max) 5.55 (Mean)	4.70 (Max) 4.69 (Mean)
$\max_{\omega}\lvert \boldsymbol{S}(j\omega)\rvert$ **(dB)**	<6 dB	13.11 (Max) 6.69 (Mean)	12.05 (Max) 6.60 (Mean)	6.24 (Max) 5.48 (Mean)

For the position transfer functions, the three controllers exceed the 0.01 Hz recommendation (two and even four times depending on the controller and the axis). However, the flexible modes mostly affect the attitude transfer functions and do not impose such strong constraints on the position transfer functions. Consequently, it is possible to go over 0.01 Hz for the position loops, as is proved by the satisfying time domain results in Table V.

For the attitude transfer functions, the open-loop cross-over frequencies are around 0.01 Hz for the H-infinity and for both the non-diagonal and diagonal MIMO QFT designs.

3.6.4 Control Requirements

Stability Objectives

Stability and performance specifications are essentially described as mathematical expressions ready to be used during the design process of the controller. These expressions usually differ from one control methodology to another provided they are based on distinct approaches, which is the case of H-infinity and QFT-based methodologies. In this paper the stability specifications have been defined in two different ways:

a) Stability conditions of Section 2.6 for MIMO QFT (Nyquist criterion for sequential methods).
b) Margins on $\max_{\omega}\lvert \boldsymbol{T}(j\omega)\rvert$ and $\max_{\omega}\lvert \boldsymbol{S}(j\omega)\rvert$ for H-infinity (classical criterion for MIMO systems).

The non-diagonal and the diagonal MIMO QFT controllers fulfill the stability conditions for sequential procedures defined in Section 2.6. The H-infinity compensator fulfills the margins of $\boldsymbol{T}(s)$ and $\boldsymbol{S}(s)$ defined in Table VI. With respect to this classical interpretation of robust stability, the QFT approaches respect them in most of the cases (mean), but not in several cases (max). This is due to the fact that these interpretations of the stability margins (which are indeed a margin of a margin) are not integrated as a design specification in the core of QFT techniques.

Since stability and performance specifications are only interpretations of the functional requirements (astronomical and engineering requirements –Table IV-), the designer should be aware of which tradeoffs need to be made. Essentially, the interpretation of reality in terms of a particular theory can never replace the real world itself. In the absence of the real system implementation or a suitable prototype to be used instead, the designer must manage time domain simulations in order to verify the control system behavior [1]. That interpretation was done and successfully validated in the previous sections of the paper.

Additionally, the classical margins on $\max_{\omega}|\boldsymbol{T}(j\omega)|$ and $\max_{\omega}|\boldsymbol{S}(j\omega)|$ are stability MIMO margins, but they do not include phase information. This fact makes them sufficient, but not necessary conditions and could yield very conservative controllers in some situations. Although the three methods are robust stable according to their own requirement and to time domain simulations, future research work to re-interpret both types of robust stability conditions and margins constitute one of the next research objectives.

Controller Complexity and Order

The number of operations that have to be performed per sampling period may place restrictions on the compensator design. The implementation of a controller based on the state space representation differs from that based on transfer functions. The former appears to have a common denominator for every element of the compensator when it is transformed into transfer function description and the latter does not actually need it. Indeed, the expression of each control signal in a transfer function matrix depends on its corresponding row of the compensator matrix. But even there, common denominators are not needed. The control signal $u_i(s)$ is computed as the sum of signals generated by every compensator in the *i*-th row.

In order to make a realistic comparison of the computational cost of the different controllers (non-diagonal MIMO QFT, H-infinity and diagonal MIMO QFT), the number of sums and multiplications computed in each sample at the final implementation are analyzed. Following the same discretization process, the values in Table VII are obtained. The compensator matrix of the H-infinity design expressed in transfer function description presents 36 elements having 42nd order. The diagonal MIMO QFT design consists of six diagonal compensators going from 5th to 14th order. The non-diagonal MIMO QFT design consists of eight compensators going from 3rd to 14th order.

Table VII. Computational cost per sampling for the three controllers

Controller	Number of Multiplications	Number of Sums
Non-diagonal MIMO QFT	130	124
H-infinity	2994	2988
Diagonal MIMO QFT	116	110

4.0 COMBINING SWITCHING & ROBUST QFT CONTROL STRATEGIES TO IMPROVE CLASSICAL CONTROL[8]

This section introduces a methodology to design a family of robust controllers able to go beyond the classical linear limitations. Combining robust designs and stable switching, the new controllers optimize the time response of the system by fast adaptation of the controller parameters during the transient response according to certain rules based on the amplitude of the error. The methodology is based on both a new graphical stability criterion for switching linear systems and the robust quantitative feedback theory (QFT).

4.1 Introduction

Switching control has demonstrated to be an efficient tool in achieving tight performance specifications in control systems [15-16]. The way to reach this enhancement is by designing various parallel controllers with different characteristics, and continuously selecting among them the one that governs the system (Fig. 21). Thus, performance specifications that are not achievable by a simple linear controller, as the limitation theory predicts [17-18], can be attained through suitable switching rules.

One of the main issues in switching control techniques is that the system stability is not assured *a priori*, even if the switching is made between stable controllers. This is the reason why most of the current literature about switching systems is still devoted to stability issues. See [19-20] for general results about stability criteria applied in some particular cases.

4.2 Switching & robust QFT control

4.2.1 Switching Systems Stability

Fig. 21 shows a general scheme of a switching system. A set of controllers is designed and a supervisor selects the most suitable one, depending on the system and environment parameters.

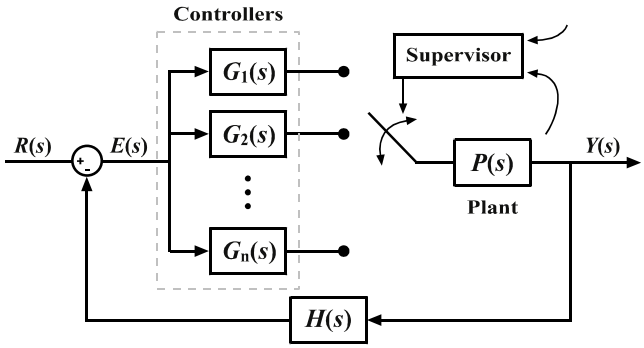

Fig. 21 Switching control scheme.

One of the main difficulties found when switching techniques are applied is that, in general, the system stability is not assured, even if switching is made between stable controllers. Some extra conditions must be met. In particular, it has been proved that a system

$$\dot{x}(t) = \mathbf{A}(t)x(t), \quad \mathbf{A}(t) \in \mathbf{A} = \{\mathbf{A}_1, ..., \mathbf{A}_m\}, \quad \mathbf{A}_i \text{ Hurwitz}, \tag{71}$$

with arbitrary switching within the set of matrices $\mathbf{A}$ is exponentially stable if and only if there exists a common Lyapunov function (CLF) for all $\mathbf{A}_i$ in the set $\mathbf{A}$ [22]. It has also been proved that the existence of a common quadratic Lyapunov function (CQLF) is a sufficient condition for exponential stability [23]. In this context, the main issue in linear switching systems is finding conditions under which the existence of a CQLF is assured. In particular, it has been proved that the circle criterion provides necessary and sufficient conditions for the existence of a CQLF for two systems in companion form [24-26], that is, the systems

$$\dot{x}(t) = \mathbf{A}x(t) \tag{72}$$

$$\dot{x}(t) = (\mathbf{A} - \mathbf{g}\boldsymbol{\Delta}^T)x(t) \tag{73}$$

both Hurwitz, with

$$\boldsymbol{A}=\begin{bmatrix} 0 & 1 & 0 & \cdots & 0 & 0 \\ 0 & 0 & 1 & \cdots & 0 & 0 \\ 0 & 0 & 0 & \cdots & 0 & 0 \\ \vdots & \vdots & \vdots & \ddots & \vdots & \vdots \\ 0 & 0 & 0 & \cdots & 0 & 1 \\ -e_0 & -e_1 & -e_2 & \cdots & -e_{n-2} & -e_{n-1} \end{bmatrix}, \quad \boldsymbol{g}=\begin{bmatrix} 0 \\ 0 \\ 0 \\ \vdots \\ 0 \\ 1 \end{bmatrix}, \quad \boldsymbol{\Delta}=\begin{bmatrix} \Delta e_0 \\ \Delta e_1 \\ \Delta e_2 \\ \vdots \\ \Delta e_{n-2} \\ \Delta e_{n-1} \end{bmatrix} \tag{74}$$

have a CQLF if and only if

$$1+\mathrm{Re}\{\boldsymbol{\Delta}^T(s\mathbf{I}-\mathbf{A})^{-1}\mathbf{g}\}>0, \quad s=j\omega, \quad \text{for all frequency } \omega. \tag{75}$$

This paper considers stability for arbitrary switching between two closed-loop systems with transfer functions $T_1(s) = L_1(s)/[1+L_1(s)]$ and $T_2(s) = L_2(s)/[1+L_2(s)]$, both stable, where $L_1(s) = P(s)G_1(s)$ and $L_2(s) = P(s)G_2(s)$ are proper, have the same number of poles, and the same number of zeros. In this case, the effect of switching is to change the gain and the position of poles and zeros. The open loop transfer functions of both systems are

$$L_1(s)=\frac{b_{n-1}s^{n-1}+\ldots+b_0}{s^n+a_{n-1}s^{n-1}+\ldots+a_0}=\frac{N(s)}{D(s)} \qquad \text{and} \tag{76}$$

$$L_2(s)=\frac{(b_{n-1}+\Delta b_{n-1})s^{n-1}+\ldots+(b_0+\Delta b_0)}{s^n+(a_{n-1}+\Delta a_{n-1})s^{n-1}+\ldots+(a_0+\Delta a_0)}=\frac{N(s)+\Delta N(s)}{D(s)+\Delta D(s)}. \tag{77}$$

Note: For the sake of clarity in the subsequent analysis, a general expression has been used where the order or the numerator is one less than that of the denominator. If it were not the case, then the coefficients b_{n-1}, etc, would be zero.

The closed-loop transfer functions are

$$T_1(s)=\frac{L_1(s)}{1+L_1(s)}=\frac{N(s)}{D(s)+N(s)} \qquad \text{and} \tag{78}$$

$$T_2(s)=\frac{L_2(s)}{1+L_2(s)}=\frac{N(s)+\Delta N(s)}{D(s)+\Delta D(s)+N(s)+\Delta N(s)}, \tag{79}$$

where the characteristic equations are

$$D(s)+N(s)=s^n+e_{n-1}s^{n-1}+\ldots+e_1s+e_0 \qquad \text{and} \tag{80}$$

$$D(s)+\Delta D(s)+N(s)+\Delta N(s)=s^n+(e_{n-1}+\Delta e_{n-1})s^{n-1}+\ldots+(e_0+\Delta e_0), \tag{81}$$

with $e_i=a_i+b_i$ and $\Delta e_i=\Delta a_i+\Delta b_i$.

Using these expressions for the coefficients e_i and Δe_i, the matrices **A**, **g**, and **Λ** are defined. Now the circle criterion is applied to guarantee stability under arbitrary switching. As

$(s\mathbf{I}-\mathbf{A})^{-1} = s^n + e_{n-1}s^{n-1} + ... + e_1 s + e_0$ and $\mathbf{\Lambda}^T\mathbf{g} = \Delta e_{n-1}s^{n-1} + ... + \Delta e_1 s + \Delta e_0$, (75) becomes

$$1 + \mathrm{Re}\left\{\frac{\Delta e_{n-1}s^{n-1} + ... + \Delta e_1 s + \Delta e_0}{s^n + e_{n-1}s^{n-1} + ... + e_1 s + e_0}\right\} > 0,\ s = j\omega,\ \text{for all frequency } \omega. \tag{82}$$

After some simple manipulation,

$$\mathrm{Re}\left\{1 + \frac{\Delta e_{n-1}s^{n-1} + ... + \Delta e_1 s + \Delta e_0}{s^n + e_{n-1}s^{n-1} + ... + e_1 s + e_0}\right\} = \mathrm{Re}\left\{\frac{N(s) + \Delta N(s) + D(s) + \Delta D(s)}{N(s) + D(s)}\right\} =$$

$$= \mathrm{Re}\left\{\frac{\dfrac{N(s) + \Delta N(s) + D(s) + \Delta D(s)}{N(s) + \Delta N(s)}}{\dfrac{N(s) + D(s)}{N(s)}}\left(\frac{N(s) + \Delta N(s)}{N(s)}\right)\right\} = \mathrm{Re}\left\{\frac{1 + L_2(s)}{1 + L_1(s)}\left(\frac{D(s) + \Delta D(s)}{D(s)}\right)\right\} \tag{83}$$

the condition can be expressed in the following form:

$$\mathrm{Re}\left\{\frac{1 + L_2(s)}{1 + L_1(s)}\left(\frac{D(s) + \Delta D(s)}{D(s)}\right)\right\} > 0,\ s = j\omega,\ \text{for all frequency } \omega. \tag{84}$$

As this formulation of the circle criterion is applied to open-loop transfer functions, it is enough to check it at positive frequencies due to symmetry. Condition (84) is then equivalent to

$$\left|\arg\{1 + L_2(j\omega)\} - \arg\{1 + L_1(j\omega)\} + \arg\left\{\frac{D(j\omega) + \Delta D(j\omega)}{D(j\omega)}\right\}\right| < \frac{\pi}{2} \ \text{for all}\ \omega \geq 0. \tag{85}$$

Let us denote

$$\varphi_{12}(\omega)[\mathrm{deg}] = \left|\arg\{1 + L_2(j\omega)\} - \arg\{1 + L_1(j\omega)\}\right|, \tag{86}$$

$$\alpha(\omega)[\mathrm{deg}] = \left|\arg\left\{\frac{D(j\omega) + \Delta D(j\omega)}{D(j\omega)}\right\}\right|. \tag{87}$$

Using the triangle inequality, a sufficient condition for (85) is

$$\varphi_{12}(\omega) < 90 - \alpha(\omega)\ \text{deg for all}\ \omega \geq 0. \tag{88}$$

Then, the criterion can be applied graphically in both the Nyquist and the Nichols diagrams. In the first case, the criterion may be expressed by saying that $L_1(j\omega)$ and $L_2(j\omega)$ must be inside of an arc of [90 – α(ω)] deg around the point (-1,0) at each frequency. In the Nichols diagram a condition over angles

is more easily checked: plotting the frequency response of $[1 + L_1(j\omega)]$ and $[1 + L_2(j\omega)]$, the distance $\varphi_{12}(\omega)$ on the horizontal axis at each frequency must be less than $[90 - \alpha(\omega)]$ deg.

It must be noted that the function $\alpha(\omega)$ can be expressed in the following form:

$$\alpha(\omega) = \left|\arg\left\{\frac{D(j\omega)+\Delta D(j\omega)}{D(j\omega)}\right\}\right| = \left|\arg\left\{\frac{\prod_{j=1}^{n}(j\omega+p_j+\Delta p_j)}{\prod_{j=1}^{n}(j\omega+p_j)}\right\}\right| = \left|\sum_{j=1}^{n}\arg\{j\omega+p_j+\Delta p_j\}-\arg\{j\omega+p_j\}\right| \quad \textbf{(89)}$$

so it may be considered as a measurement of the controller poles change, as Fig. 22 shows. Consequently, the larger the movement made by the poles, the bigger the conservativeness introduced by the triangle inequality at (88). Note that for each frequency ω_i there is a different angle $\alpha(\omega_i)$.

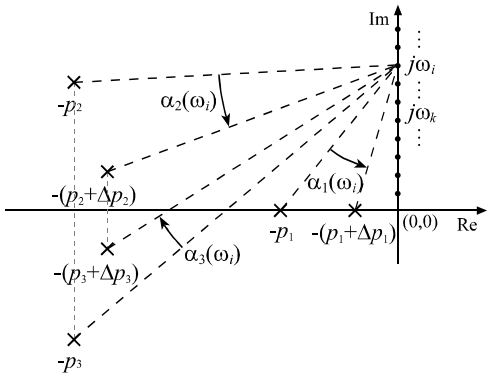

Fig. 22 $\alpha(s)$ for a system with three switching poles. $\alpha(\omega_i) = \alpha_1(\omega_i) + \alpha_2(\omega_i) + \alpha_3(\omega_i)$.

At this point two questions arise. Firstly, the criterion presented above can be applied to switching between two isolated controllers with the same structure. However, it is possible that the designer wants to do switching among more than one system, or even among an infinite number of systems, which can also be considered as a linear parameter varying (LPV) system, where the controller varies continuously. Secondly, real systems present uncertainty, so the criterion must be modified in some way to take the uncertainty into account. The next discussion undertakes both issues.

If the switching is made among a set of controllers, the criterion has to be accomplished by every pair of them. Checking this condition may be an impossible task if there is more than one pole moving, because the angle α is different for each pair of controllers. For this reason, if we are interested in a controller whose parameters change continuously with the error, we will permit only variable gain and zeros. Then, the angle $\alpha(\omega)$ is null for every frequency, and the only condition to satisfy is that the angle between any two possible systems $L_i(j\omega)$ and the critical point (-1,0) is less than 90 deg. Moreover, under this premise the conservativeness introduced in (88) vanishes. The condition can be checked graphically with a grid of the possible open-loop systems that the controller variation can generate, as Fig. 23a shows. The maximum angle $\varphi_{12}(\omega)$ must be contained in a 90 deg arc from (-1,0). In the Nichols Plot, the way to apply the criterion is to draw the grid of possible $1+L_i(j\omega)$ systems, and check that the maximum horizontal distance is less than 90 deg. Fig. 23b illustrate the criterion in the Nichols Plot.

Using similar arguments, it is also easy to deal with uncertainty. For an uncertain system, the *template* $\Im\mathbf{P}(j\omega)$ is the area of the possible plants within the uncertainty at the frequency ω. If this system is governed by a switching controller, each point of the template can change its position due to switching. From this point of view, switching can be considered as a mechanism that modifies the position and shape of the templates of $[1 + L_i(j\omega)]$. To be sure that the switching is stable, the above criterion must be applied to the whole template.

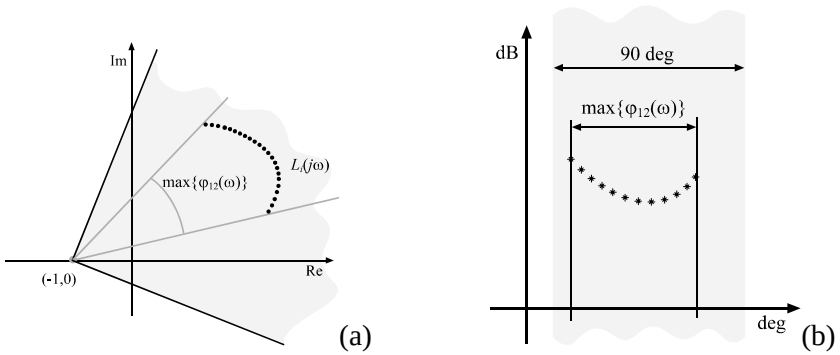

Fig. 23 Criterion for continuous switching: a) Complex plane. b) Nichols plot.

It has been traditionally considered in control theory that uncertainty changes the plant slowly in comparison with the system dynamics. If the switching laws depend on the state of the system, then the switching is much faster than changes due to uncertainty. Consequently, for each point of the departure template there is only one corresponding point in the arrival template. Furthermore, it can be assumed that uncertainty does not affect the angle α.

Then the Nichols Chart is a very clear diagram to test the stability of the uncertain switching system. Fig. 24 shows the templates of $[1+L_i(j\omega)]$ and the application of the method. If during the displacement of each point of the first template to its corresponding point of the second one, the maximum horizontal distance between any two points of this path is less that 90 deg, the stability condition is satisfied at that particular frequency. Although it is a laborious task to check each point of the template at each frequency, usually it is not necessary because the whole set of templates are much closer together than the critical distance.

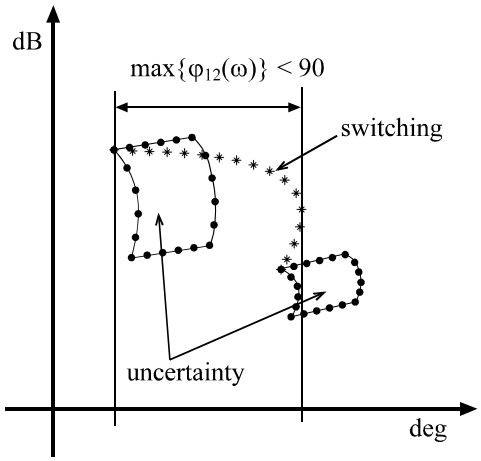

Fig. 24 Stability criterion on the Nichols Chart

4.2.2 Methodology

Quantitative feedback theory [1] has demonstrated to be an excellent tool dealing with the compromises between several, often conflicting, control specifications. Its transparent design process allows the designer to consider all of them simultaneously and in the same plot. The QFT philosophy permits to design a controller that satisfies the set of performance specifications with every plant within the uncertainty, using the minimum amount of feedback.

However, as any linear methodology, QFT produces linear controllers, and consequently it is subject to the performance limitations of linear systems. Briefly speaking, the way in which a system can improve its performance is limited by the reduction of the stability margins. Although those limitations are usually expressed in the frequency domain, they have consequences in the time response of the system.

As limitations are due to the linear character of the system, it seems that the key is to use nonlinear controllers. Some work has been done in that respect, and some elegant solutions have been performed [27-28]. However, the use of nonlinear elements may imply some problems, like instability or limit cycles, as well as the lack of simple design tools.

Another solution to overcome the linear limitations is to prioritize some specifications over others according to the state of the system at each time. In other words, do switching to select the appropriate controller, keeping always the linear character. A particular way to do this is to use the error amplitude as the switching signal. Then, when the output is far from the reference, the system needs to be more stable, and also faster, but precision is not so necessary. Conversely, when there is little error, some amount of stability margin can be sacrificed in order to increase the low frequency gain, and therefore the precision and the disturbance rejection. These ideas, combined with the QFT method, lead to a new design procedure, listed in the next four steps:

Step 1: Obtain a preliminary linear controller for the system, usually by applying QFT: represent the parametric and/or non-parametric uncertainty with the templates, define the frequency domain specifications, generate the QFT-bounds and design a linear controller by loop-shaping.

Step 2: The preliminary QFT controller is the starting point to design two extreme controllers with the same structure, where gain and zeros can vary freely, but poles stand still. The characteristics of these two controllers must be related with the error amplitude. As Boris Lurie explains [16], when the error is large the bandwidth must increase to get fast response, but the loop gain does not need to be high. And for small errors, the bandwidth is reduced to avoid the effects of noise, while the low frequency gain is increased to minimize the jitter and the tracking error.

In terms of loop-shaping, these rules can be considered as: 1) for small errors, increase gain and move further away the zeros, and 2) for high errors, decrease gain and bring nearer the zeros. Apart from this, reasonable stability margins must be maintained, although they could be considerably reduced for the small error situation.

Step 3: The robustness of the extreme designs guarantees that both linear systems are stable for every plant within the uncertainty. However, it is necessary to apply the criterion presented in the previous section [see equation (88) with $\alpha = 0$] to assure that the switching between both controllers is also stable.

One advantage of this graphical criterion is that it gives information about the frequencies where conditions are not satisfied, so the designer can go back to Step 2 and change the extreme controllers in this region.

Step 4: Select the switching function. Simulations of the system governed by each controller are performed. Looking at the time response of the designs, the function that relates the error amplitude with the position of the controller parameters is designed (see for example Fig. 27).

4.3 Application: Remotely Controlled Reconnaissance Vehicle

This section presents a simple example to illustrate the new methodology introduced in section 4.2. It consists in a remotely controlled reconnaissance vehicle (see [29] for details).

The plant to be controlled is:

$$P(s) = \frac{1}{\left(s^2 + a_1 s + a_0\right)}; \text{where } a_1 \in [1.8, 2.2], \text{ and } a_0 \in [3.6, 4.4] \quad \textbf{(90)}$$

Step 1
The controller designed by Dorf (see [29]) is:

$$G_0(s) = \frac{10(s+2)}{(s+1)} \quad \textbf{(91)}$$

Step 2
Now, starting from $G_0(s)$, the extreme controllers $G_1(s)$ and $G_2(s)$, for low and high errors respectively, are designed observing the guidelines exposed in section 4.2. The elements to be varied are the gain and a zero. The new controllers are

$$G_1(s) = \frac{15(s+2.3)}{(s+1)} \quad \text{and} \quad \textbf{(92)}$$

$$G_2(s) = \frac{8(s+0.5)}{(s+1)} \quad \textbf{(93)}$$

and their frequency domain characteristics can be viewed in the Bode plot of Fig. 25. As is appreciated, $G_1(s)$ presents a higher low-frequency gain and a dominant pole, while in $G_2(s)$ the low-frequency gain is lower and the zero is the dominant one. Their robust stability margins are checked with QFT tools.

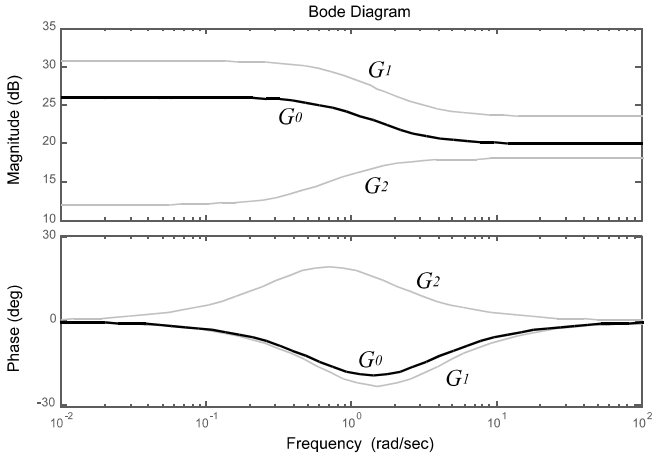

Fig. 25 Bode plot of the three controllers

Step 3

Fig. 26 shows the templates $T[1 + L_1(j\omega)]$ and $T[1 + L_2(j\omega)]$ at various representative frequencies [1, 2, 3, 5] rad/sec, and the Nichols plot of each nominal function $[1 + L_{i0}(j\omega)]$. As there is no variation in any pole of the controller, the angle α is cero for all frequencies, and the only thing to check is that, in the path from each point of the first template to its corresponding point of the second template, the maximum horizontal distance between two points is not higher than 90 deg [see (88) with $\alpha = 0$].

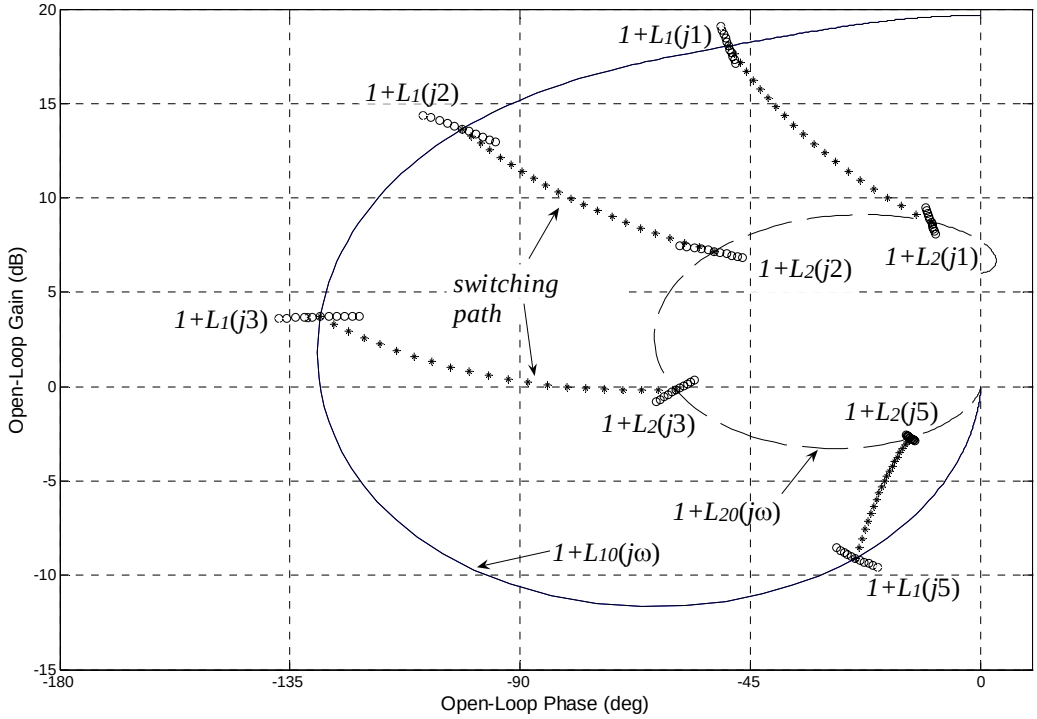

Fig. 26 Stability study of the switched systems on the Nichols chart

Step 4

The switching controller $G_{swi}(s)$ presents the following expression:

$$G_{swi}(s) = \frac{(15 - 7k)(s + 2.3 - 1.8k)}{(s + 1)} \qquad \textbf{(94)}$$

where the parameter k is given by a function $\measuredangle \rightarrow [0, 1]$ of the error signal. In order to reduce possible impulse effects, a smooth function (95) has been selected instead of a relay-type or saturation-type function,

$$k = 1 - \exp\left(-\frac{e(t)^2}{0.15}\right) \qquad \textbf{(95)}$$

where the values of the parameters have been adjusted for optimal performance by simulation. Some further research could be devoted to finding the optimum shape for the switching functions. The shape of the switching function is shown in Fig. 27.

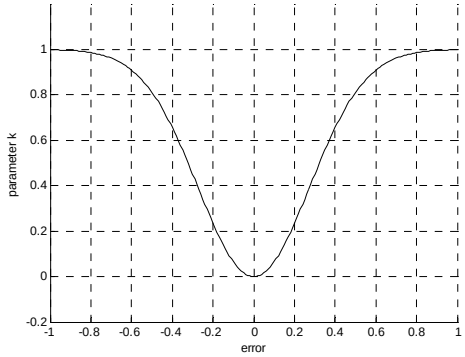

Fig. 27. Switching function

Validation

The compensators are verified in the time domain for the most representative plants selected from the set of uncertain plants. Fig. 28 shows the time response of the control system (nominal plant [29]) to a step input reference tracking (t = 1 sec) and a step disturbance (t = 15 sec). The response of the controller designed with the new methodology (switching controller, G_{swi}) combine the best characteristics of the extreme controllers (G_1 and G_2), improving the response of the original fixed controller (G_0).

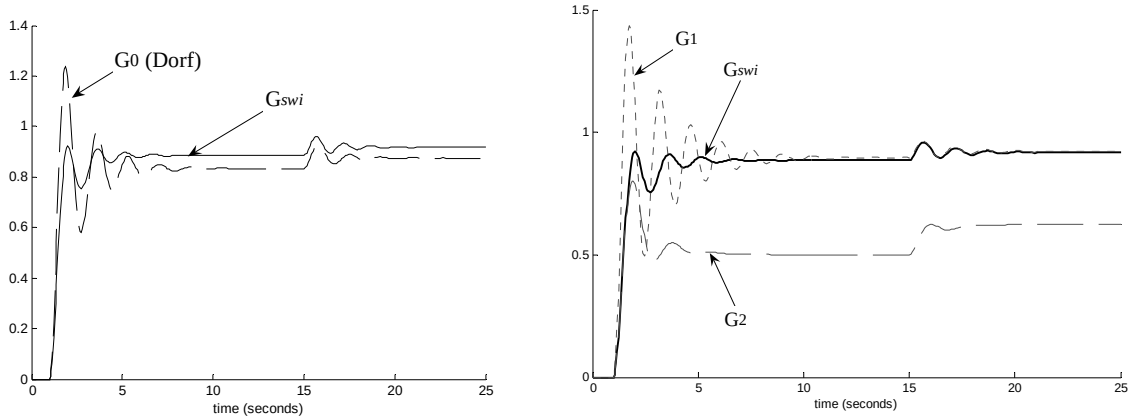

Fig. 28 Response to a step input reference tracking and a step disturbance

5.0 CONCLUSIONS

Since the very first ideas suggested by Horowitz in 1959 until now, the Quantitative Feedback Theory (QFT) has been successfully applied to many control systems: linear and non-linear, stable and unstable, SISO and MIMO, minimum and non-minimum phase, with time-delay, with lumped and distributed parameters, multi-loop, etc [1]. The method searches for the controller that guarantees the achievement of the required performance specifications for every plant within the existing model uncertainty. QFT highlights the trade-off (*quantification*) among the simplicity of the controller structure, the minimization of the 'cost of feedback', the quantified model uncertainty and the achievement of the desired performance specifications at every frequency of interest.

The first part of the paper summarized a methodology to design sequential non-diagonal QFT controllers for multi-input-multi-output MIMO systems with uncertainty. The second part demonstrated the feasibility of that methodology to control UAVs, in particular the position and attitude control of a 6x6 MIMO Darwin-type spacecraft with large flexible appendages. The third part of the paper introduced a new practical methodology to design robust controllers that work under a switching mechanism. The method is

capable of optimising performance and stability simultaneously, going beyond the classical linear limitations and giving a solution for the well-known robustness-performance trade-off. Based on the frequency domain approach, the method combines a graphical stability criterion for switching linear systems and the robust quantitative feedback theory.

ACKNOWLEDGEMENT

The first part of this research was performed under ESA/ESTEC contract 19326/05/NL/LvH. The authors gratefully appreciate the support given by the Spanish “Ministerio de Educación y Ciencia” (MEC) under grant DPI’2006-15522-C02-01. Acknowledgment is also given to Dr. Christian Philippe and Dr. Samir Bennani (ESA-ESTEC), and Dr. Marta Barreras (MTorres), for their valuable contributions for the success of this work.

REFERENCES

[1]. Houpis C.H., Rasmussen S.J., Garcia-Sanz, M. (2006), *Quantitative Feedback Theory: Fundamentals and Applications*. 2nd Edition. A CRC Press book, Taylor & Francis, Florida, USA.

[2]. Garcia-Sanz M. and Egaña I., (2002), "Quantitative non-diagonal controller design for multivariable systems with uncertainty," *Int. Journal of Robust and Nonlinear Control*, vol. 12, pp. 321-333.

[3]. Garcia-Sanz M., Egaña I., and Barreras M., (2005), "Design of quantitative feedback theory non-diagonal controllers for use in uncertain multiple-input multiple-output systems," *IEE Control Theory and Applications*, vol. 152, pp. 177-187.

[4]. Garcia-Sanz M. and Barreras M., (2006), "Non-diagonal QFT controller design for a 3-input 3-output industrial Furnace," *Journal of Dynamic Systems, Measurement and Control, ASME*, vol. 128, pp. 319-329.

[5]. Garcia-Sanz M. and Eguinoa I., (2005), "Improved non-diagonal MIMO QFT design technique considering non-minimum phase aspects," 7th International Symposium on Quantitative Feedback Theory QFT and Robust Frequency Domain Methods, Lawrence, Kansas, USA.

[6]. Garcia-Sanz M., and Hadaegh F.Y. (2007), “Load-Sharing Robust Control of Spacecraft Formations: Deep Space and Low Earth Elliptic Orbits”. Special Issue: “Cooperative Control of Multiple Spacecraft Flying in Formation”, *IEE Control Theory and Applications*. vol. 154, num 02.

[7]. Garcia-Sanz M., Eguinoa I., Barreras M., and Bennani S. “Non-diagonal MIMO QFT Controller Design for Darwin-type Spacecraft with large flimsy appendages”. *Journal of Dynamic Systems, Measurement and Control, ASME*, Vol. 130, pp. 011006-1:011006-15, January 2008.

[8]. Garcia-Sanz M., and Elso J. “Beyond the linear limitations by combining Switching & QFT. Application to Wind Turbines Pitch Control Systems”. Special Issue: “Wind Turbines: New Challenges and Advanced Control Solutions”. *International Journal of Robust and Non-Linear Control*, Vol. 18, No. 12, Wiley. Accepted for publication, March 2008.

[9]. D'Azzo J.J., Houpis C.H., and Sheldon S.N. (2003), *Linear Control System Analysis and Design with Matlab*, Fifth Edition. Marcel Dekker, New York, USA.

[10]. S. Skogestad and I. Postlethwaite, *Multivariable feedback control. Analysis and design*, 2nd Edition ed. Chichester, West Sussex, England: John Wiley & Sons Ltd., 2005.

[11]. E. H. Bristol, "On a new measure of interactions for multivariable process control.," *Transactions on Automatic Control*, vol. 11, pp. 133-134, 1966.

[12]. I. Horowitz, "Improved design technique for uncertain multiple input-output feedback systems," *International Journal of Control*, vol. 36, pp. 977-988, 1982.

[13]. M. Franchek, P. Herman, and O. Nwokah, "Robust Non-diagonal Controller Design for Uncertain Multivariable Regulating Systems," *ASME Journal of Dynamic Systems Measurement and Control*, vol. 119, pp. 80-85, 1997.

[14]. J. M. De Bedout and M. A. Franchek, "Stability conditions for the sequential design of non-diagonal multivariable feedback controllers," *International Journal of Control*, vol. 75, pp. 910-922, 2002.

[15]. N. Harris Mcclamroch and I. Kolmanovsky, "Performance benefits of hybrid control design for linear and nonlinear systems," *Proceedings of the IEEE*, vol. 88, pp. 1083-1096, 2000.

[16]. A. Feuer, G. C. Goodwin, and M. Salgado, "Potential benefits of hybrid control for linear time invariant plants," presented at Proceedings of the American Control Conference, 1997.

[17]. M.M. Seron, J.H. Braslavsky, and G.C. Goodwin, *Fundamental limitations in filtering and control*, Springer, London, 1997.

[18]. I. Horowitz, *Synthesis of feedback systems*, Academic Press, New York, 1963.

[19]. Robert Shorten, Fabian Wirth, Oliver Mason, Kai Wulff and Christopher King, “Stability criteria for switched and hybrid systems”, *SIAM Review*, 2007.

[20]. D. Liberzon and A. S. Morse, "Basic problems in stability and design of switched systems," *IEEE Control Systems Magazine*, vol. 19, pp. 59-70, 1999.

[21]. R. A. Decarlo, M. S. Branicky, S. Pettersson, and B. Lennartson, "Perspectives and results on the stability and stabilizability of hybrid systems," *Proceedings of the IEEE*, vol. 88, pp. 1069-1082, 2000.

[22]. A. P. Molchanov and E. S. Pyatnitskii, “Criteria of asymptotic stability of differential and difference inclusions encountered in control theory,” *Systems & Control Letters*, vol. 13, pp. 59-64, 1989.

[23]. W. P. Dayawansa and C. F. Martin, “A converse Lyapunov theorem for a class of dynamical systems which undergo switching,” *IEEE Transactions on Automatic Control*, vol. 44, pp. 751-760, 1999.

[24]. K. Narendra and R. Goldwyn, "A Geometrical Criterion for the Stability of Certain Nonlinear Nonautonomous Systems," *IEEE Transactions on Circuits and Systems*, vol. 11, pp. 406-408, 1964.

[25]. J. Willems, "The circle criterion and quadratic Lyapunov functions for stability analysis," *IEEE Transactions on Automatic Control*, vol. 18, pp. 184, 1973.

[26]. R. N. Shorten, O. Mason, F. O'Cairbre, and P. Curran, "A unifying framework for the SISO circle criterion and other quadratic stability criteria," *International Journal of Control*, vol. 77, pp. 1-8, 2004.

[27]. B. J. Lurie and P. J. Enright, *Classical feedback control with MATLAB*, Marcel Dekker, New York, 2000.

[28]. J. W. Glass and M. A. Franchek, “Frequency-based nonlinear controller design for regulating systems subjected to time-domain constraints,” *International Journal of Robust and Nonlinear Control*, vol. 10, pp. 39-57, 2000.

[29]. R.C. Dorf and R.H. Bishop, “*Modern Control Systems*”. 11th edition, 2007, Addison Wesley.